The Astrophysical Journal, 863:166 (16pp), 2018 August 20 https://doi.org/10.3847/1538-4357/aad40e
© 2018. The American Astronomical Society. All rights reserved.

Chemo-kinematic Ages of Eccentric-planet-hosting M Dwarf Stars

Mark J. Veyette and Philip S. Muirhead
Department of Astronomy & The Institute for Astrophysical Research, Boston University, 725 Commonwealth Ave., Boston, MA 02215, USA; mveyette@bu.edu
Received 2018 May 21; revised 2018 July 9; accepted 2018 July 15; published 2018 August 22

Abstract

The M dwarf stars are exciting targets for exoplanet investigations; however, their fundamental stellar properties are difficult to measure. Perhaps the most challenging property is stellar age. Once on the main sequence, M dwarfs change imperceptibly in their temperature and luminosity, necessitating novel statistical techniques for estimating their ages. In this paper, we infer ages for known eccentric-planet-hosting M dwarfs using a combination of kinematics and α-element enrichment, both shown to correlate with age for Sun-like FGK stars. We calibrate our method on FGK stars in a Bayesian context. To measure α-enrichment, we use publicly available spectra from the CARMENES exoplanet survey and a recently developed [Ti/Fe] calibration utilizing individual Ti I and Fe I absorption lines in the Y band. Tidal effects are expected to circularize the orbits of short-period planets on short timescales; however, we find a number of mildly eccentric, close-in planets orbiting old ($\sim$8 Gyr) stars. For these systems, we use our ages to constrain the tidal dissipation parameter of the planets, $Q_{\rm p}$. For two mini-Neptune planets, GJ 176 b and GJ 536 b, we find that they have $Q_{\rm p}$ values more similar to the ice giants than to the terrestrial planets in our solar system. For GJ 436 b, we estimate an age of $8.9^{+2.3}_{-2.1}$ Gyr and constrain the $Q_{\rm p}$ to be $>10^5$, in good agreement with constraints from its inferred tidal heating. We find that GJ 876 d has likely undergone significant orbital evolution over its $8.4^{+2.2}_{-2.0}$ Gyr lifetime, potentially influenced by its three outer companions that orbit in a Laplace resonance.

Key words: planets and satellites: dynamical evolution and stability – planets and satellites: gaseous planets – stars: abundances – stars: fundamental parameters – stars: late-type – stars: low-mass

1. Introduction

M dwarf stars are small stars, with masses between $\sim$0.1 and $\sim$0.6 $M_\odot$ and radii between $\sim$0.1 and $\sim$0.6 $R_\odot$. As a spectral class, M types are defined by strong molecular features in their spectra, which are a consequence of their relatively cool photospheres with effective temperatures ranging between 2800 and 3800 K. M dwarf stars enable a variety of investigations into the role of stellar mass in exoplanet formation. For example, M dwarfs are known to host fewer Jupiter-mass planets than Sun-like FGK stars (Johnson et al. 2010a), supporting planet formation models that predict slow planetesimal growth during the protoplanetary disk phase (Laughlin et al. 2004).

Additionally, M dwarf stars enable tests of exoplanet evolution in the regime of low host-star mass. They are known to be abundant hosts of small, short-period planets (Dressing & Charbonneau 2013; Swift et al. 2013; Gaidos et al. 2014; Morton & Swift 2014; Dressing & Charbonneau 2015; Gaidos et al. 2016). Tidal interactions between a host star and its planet tend to circularize and reduce the semimajor axis of short-period orbits over time (Goldreich & Soter 1966). The timescale of this evolution depends strongly on the semimajor axis of the orbit (Jackson et al. 2008). Planet-hosting M dwarfs, with their tendency to host small planets on compact orbits, are excellent targets for investigating the role of tidal migration and circularization.

Planet orbital evolution around M dwarf stars could be investigated with measurements of M dwarf ages; however, measuring the ages of M dwarf stars is challenging. Once on the main sequence, M dwarfs move imperceptibly on a Hertzsprung–Russell or color–magnitude diagram due to their low core fusion rates, taking tens of billions of years to change by a significant degree in temperature or luminosity (Laughlin et al. 1997; Choi et al. 2016). Gyrochronology, the study of stellar spin-down versus age, holds some promise for measuring M dwarf ages (e.g., Meibom et al. 2015; Barnes et al. 2016).

However, work by Irwin et al. (2011) and Newton et al. (2016) found that field mid-M dwarfs exhibit a bimodal distribution in rotation period, similar to what is seen for Sun-like stars in young clusters (Attridge & Herbst 1992; Barnes 2003). This indicates that either slow or fast rotation is frozen in during formation, or some rapid process takes place where stars spin down suddenly from fast to slow rotation. This could be a result of a dramatic reorganizing of the magnetic field topology at some specific rotation or age (Garraffo et al. 2015, 2018). If the transition is stochastic, then gyrochronology can do little to constrain the ages of young and intermediate-age M dwarfs. The prospects for applying gyrochronology after such a transition remain to be seen.

The chemical and kinematic evolution of the Galaxy provides a new way to estimate the ages of M dwarf stars. Work by Haywood et al. (2013) showed a strong correlation between stellar age, iron abundance, and α-enhancement for nearby F-, G-, and K-type dwarfs, for which ages were measured by comparing spectroscopic parameters to stellar evolution models. Work by Bensby et al. (2014) shows similarly strong correlations between α-enhancement, specifically titanium enhancement ([Ti/Fe]), iron abundance, and age, over ages that span nearly the entire history of the universe: 1.5–13.5 Gyr. The relation between α-enhancement and stellar age is the result of early interstellar medium (ISM) enrichment of α-elements by core-collapse supernovae and delayed enrichment of iron by Type Ia supernovae. The delayed enrichment of iron causes [α/Fe] to decrease and [Fe/H] to increase over time. This trend has been confirmed by numerous

studies of solar-neighborhood FGK stars (Nissen 2015; Spina et al. 2016; Buder et al. 2018) and red giant stars (Martig et al. 2015; Feuillet et al. 2016, 2018; Hawkins et al. 2016). Recently, Bedell et al. (2018) showed that when restricting the stellar sample to only solar twins (stars with similar temperature, surface gravity, and overall metallicity to the Sun), there is an exceptionally tight relation between stellar age and the abundance of α-elements, including titanium. These age–abundance relations provide a path to statistically measure stellar ages and should apply just as well to nearby M dwarfs as to nearby F-, G-, and K-type stars.

M dwarfs' cooler photospheres allow molecules to form throughout their atmospheres. Opacity from these molecules contributes millions of absorption lines that blanket an M dwarf's optical and NIR spectrum. Difficulties in modeling cool stellar atmospheres and the millions of molecular transitions occurring in them have so far prohibited the detailed chemical analysis of M dwarfs. Empirically calibrated, model-independent methods to measure M dwarf metallicities provide a way around these issues (Bonfils et al. 2005a; Johnson & Apps 2009; Rojas-Ayala et al. 2010; Mann et al. 2013). However, these methods are indirect tracers of metallicity relying on astrophysical abundance correlations (Veyette et al. 2016) and are limited to measuring overall metallicity. Veyette et al. (2017) presented a new physically motivated and empirically calibrated method to measure the effective temperature, iron abundance, and titanium enhancement of an M dwarf from its high-resolution Y-band spectrum around 1 μm. With the ability to measure the [Ti/Fe] of M dwarfs, we can now apply the well-studied [Ti/Fe]–age relation to estimate the ages of M dwarfs.

In this paper, we estimate ages for eccentric-planet-hosting M dwarf stars by combining galactic kinematics with titanium enhancement. In Section 2, we describe how the sample of planet hosts was chosen and the high-resolution NIR spectra used in this work. In Section 3, we describe how we measured the [Ti/Fe] of these M dwarfs from their high-resolution Y-band spectra and used a sample of FGK stars with measured [Ti/Fe] and ages to calibrate an empirical, probabilistic [Ti/Fe]–age relation. In Section 4, we combine our [Ti/Fe]–age relation with a kinematic prior to estimate ages for our sample of planet-hosting M dwarfs. In Section 5, we use our ages to explore the tidal evolution of the planets and constrain their tidal Q. Finally, we summarize this work in Section 6.

2. Sample

The Calar Alto high-Resolution search for M dwarfs with Exo-earths with Near-infrared and optical chelle Spectrographs (CARMENES) is a high-resolution optical and NIR spectroscopic survey to search for rocky planets in the habitable zones of nearby M dwarfs (Quirrenbach et al. 2014). The CARMENES spectrograph covers 0.5–1.7 μm at a resolution of 94,600 in the optical and 80,400 in the NIR. Reiners et al. (2018b, hereafter R18) published one representative CARMENES spectrum for each of the 324 M dwarfs in the survey.

We downloaded the NIR spectra for all 324 CARMENES GTO targets from the CARMENES GTO Data Archive (Caballero et al. 2016).[1] Many of the spectra exhibit large, spurious features that are likely a result of the automatic flat-relative extraction pipeline used by CARMENES (Zechmeister et al. 2014). We checked each spectrum by eye in the Y-band region and excluded from further analysis any spectrum that contains either large spikes spanning over 100 pixels that are present in multiple orders or large, sharp variations in the continuum that make it impossible to consistently assess the pseudo-continuum across the full Y band. Roughly half the spectra did not meet our quality cuts. We also excluded stars with projected rotational velocity $v \sin i > 12$ km s^{-1}, corresponding to the resolution of the NIRSPEC spectra used to calibrate the Veyette et al. (2017) method.

We cross-matched the stars the passed our quality cuts and that had masses $>0.2\ M_\odot$ with the NASA Exoplanet Archive.[2] We found 11 M dwarfs that host known exoplanets: GJ 176 b (Forveille et al. 2009), GJ 179 b (Howard et al. 2010), GJ 436 b (Butler et al. 2004), GJ 536 b (Suárez Mascareño et al. 2017a), GJ 581 b, c, e (Bonfils et al. 2005b; Udry et al. 2007; Mayor et al. 2009), HD 147379 b (GJ 617 A, Reiners et al. 2018a), GJ 625 b (Suárez Mascareño et al. 2017b), Wolf 1061 b, c, d (GJ 628, Wright et al. 2016), GJ 649 b (Johnson et al. 2010b), GJ 849 b (Butler et al. 2006), and GJ 876 b, c, d, e (Marcy et al. 1998, 2001; Rivera et al. 2005, 2010). Table 1 lists the exoplanets analyzed in this study and their relevant parameters.

Table 1
Planet-hosting M Dwarf Exoplanet Parameters

Planet	$M_p \sin i$ ($M_\oplus$)	a (au)	e	References
GJ 176 b	$9.06^{+1.54}_{-0.7}$	$0.066^{+0.001}_{-0.001}$	$0.148^{+0.249}_{-0.036}$	(1)
GJ 179 b	$260.61^{+22.25}_{-22.25}$	$2.41^{+0.04}_{-0.04}$	$0.21^{+0.08}_{-0.08}$	(2)
GJ 436 b	$21.36^{+0.2}_{-0.21}$	$0.028^{+0.001}_{-0.001}$	$0.152^{+0.009}_{-0.008}$	(1)
GJ 536 b	$6.52^{+0.69}_{-0.4}$	$0.067^{+0.001}_{-0.001}$	$0.119^{+0.125}_{-0.032}$	(1)
GJ 581 b	$15.2^{+0.22}_{-0.27}$	$0.041^{+0.001}_{-0.001}$	$0.022^{+0.027}_{-0.005}$	(1)
GJ 581 c	$5.652^{+0.386}_{-0.239}$	$0.074^{+0.001}_{-0.001}$	$0.087^{+0.15}_{-0.016}$	(1)
GJ 581 e	$1.657^{+0.24}_{-0.161}$	$0.029^{+0.001}_{-0.001}$	$0.125^{+0.078}_{-0.015}$	(1)
GJ 617 A b	$24.7^{+1.8}_{-2.4}$	$0.3193^{+0.0002}_{-0.0002}$	$0.01^{+0.12}_{-0.01}$	(3)
GJ 625 b	$2.82^{+0.51}_{-0.51}$	$0.078361^{+4.4e-05}_{-4.6e-05}$	$0.13^{+0.12}_{-0.09}$	(4)
GJ 628 b	$1.91^{+0.26}_{-0.25}$	$0.0375^{+0.0012}_{-0.0013}$	$0.15^{+0.13}_{-0.1}$	(5)
GJ 628 c	$3.41^{+0.43}_{-0.41}$	$0.089^{+0.0029}_{-0.0031}$	$0.11^{+0.1}_{-0.07}$	(5)
GJ 628 d	$7.7^{+1.12}_{-1.06}$	$0.47^{+0.015}_{-0.017}$	$0.55^{+0.08}_{-0.09}$	(5)
GJ 649 b	$104.244^{+10.17}_{-10.17}$	$1.135^{+0.035}_{-0.035}$	$0.3^{+0.08}_{-0.08}$	(6)
GJ 849 b	289.21	2.32	$0.05^{+0.03}_{-0.03}$	(7)
GJ 876 b	$760.9^{+1.0}_{-1.0}$	$0.214^{+0.001}_{-0.001}$	$0.027^{+0.002}_{-0.002}$	(1)
GJ 876 c	$241.5^{+0.7}_{-0.6}$	$0.134^{+0.001}_{-0.001}$	$0.25^{+0.001}_{-0.002}$	(1)
GJ 876 d	$6.91^{+0.22}_{-0.27}$	$0.021^{+0.001}_{-0.001}$	$0.082^{+0.043}_{-0.025}$	(1)
GJ 876 e	$15.43^{+1.29}_{-1.27}$	$0.345^{+0.001}_{-0.002}$	$0.04^{+0.021}_{-0.004}$	(1)

Note. Here M_p is used when i is known. References: (1) Trifonov et al. (2018), (2) Howard et al. (2010), (3) Reiners et al. (2018a), (4) Suárez Mascareño et al. (2017b), (5) Astudillo-Defru et al. (2017), (6) Johnson et al. (2010a), (7) Bonfils et al. (2013).

3. Analysis

3.1. Measuring [Ti/Fe]

We employed the method developed by Veyette et al. (2017) to measure the $T_{\rm eff}$, [Fe/H], and [Ti/Fe] of the M dwarfs in our sample from the Y-band region of their high-resolution CARMENES spectra. The method utilizes strong, relatively isolated Fe and Ti lines in the Y band to directly estimate Fe

[1] http://carmenes.cab.inta-csic.es/

[2] https://exoplanetarchive.ipac.caltech.edu/

Table 2
Planet-hosting M Dwarf Stellar Parameters

Name	U (km s^{-1})	V (km s^{-1})	W (km s^{-1})	$T_{\rm eff}$ (K)	[Fe/H]	[Ti/Fe]	Age (Gyr)
GJ 176	−22.6	−56.7	−14.8	3538	+0.05	+0.04	$8.8^{+2.5}_{-2.8}$
GJ 179	+13.3	−17.2	+0.9	3350	+0.12	+0.06	$4.6^{+3.5}_{-2.4}$
GJ 436	+52.0	−19.2	+19.5	3466	−0.08	+0.07	$8.9^{+2.3}_{-2.1}$
GJ 536	−54.6	+2.3	+2.9	3653	−0.12	+0.06	$6.9^{+2.5}_{-2.3}$
GJ 581	−25.0	−25.4	+11.6	3377	+0.06	+0.04	$6.6^{+2.9}_{-2.5}$
GJ 617 A	−9.9	−30.1	+4.0	3966	+0.13	−0.00	$5.1^{+3.2}_{-2.4}$
GJ 625	+7.8	−2.6	−17.6	3433	−0.37	+0.12	$7.0^{+2.7}_{-4.1}$[a]
GJ 628	−13.0	−21.1	−20.6	3456	−0.25	−0.02	$4.3^{+3.1}_{-2.0}$
GJ 649	+21.3	−14.3	+1.2	3595	+0.03	−0.02	$4.5^{+3.0}_{-2.0}$
GJ 849	−44.6	−17.6	−17.6	3469	+0.28	−0.01	$4.9^{+3.0}_{-2.1}$
GJ 876	+1.3	−2.2	−49.9	3295	+0.18	+0.02	$8.4^{+2.2}_{-2.0}$

Notes. Ages are posterior medians and $\pm1\sigma$ values corresponding to the 16th and 84th percentiles.
[a] See discussion in Section 5.2.7.

and Ti abundances. The method is physically motivated, using a custom grid of PHOENIX BT-Settl models (Allard et al. 2012; Baraffe et al. 2015; Allard 2016) to provide the nonlinear relations for how M dwarf spectra change as a function of temperature and composition. It is also empirically calibrated by using observations of widely separated FGK and M-type binary stars to derive corrections to the model relations, ensuring agreement between abundance analyses of solar-type stars and M dwarfs.

The Veyette et al. (2017) method was originally calibrated on Keck/NIRSPEC spectra at a resolution of 25,000. Due to severe blending with neighboring molecular lines, the calibration is only valid when applied to spectra at the same resolution. We took the following steps to prepare the CARMENES spectra and closely match the format of the NIRSPEC spectra used in the original calibration. First, we masked out pixels 300–370 in the third and fourth orders of the NIR spectra. Most spectra had broad peaks at these pixel locations, which we assume are an artifact of the reduction process. Next, to remove a number of large narrow spikes that appear at random pixel locations throughout many of the spectra, we masked out pixels with flux values that were more than five median absolute deviations greater than the median flux value of the 200 surrounding pixels. We then interpolated the spectra to a finer grid with uniform log spacing in wavelength and convolved them down to a resolution of 25,000. Finally, to remove edge effects from the discrete convolution, we masked out pixels within ±2.5 times the convolution kernel FWHM of the edge of each order or the chip gap at the 2040th pixel location.

We followed the same procedure outlined in Veyette et al. (2017) to correct the shape of each order and set the pseudo-continuum level. We excluded the 1.05343–1.05360 μm Fe line and the 1.07285–1.07300 μm Ti line from our analysis, as they fall too close to the chip gap and were masked out in some spectra. We also changed the FeH index defined in Veyette et al. (2017) to be the ratio of the flux in the 0.988–0.9895 and 0.990–0.992 μm regions. The original definition of the FeH index covered the chip gap and a transition from one order to the next. We used the calibration sample from Veyette et al. (2017) to recalculate the empirical corrections for this modified feature list. The accuracy of the calibration is similar to that achieved with the original feature list. The root-mean-square error (RMSE) of the inferred parameters of our calibration sample are 56 K in $T_{\rm eff}$, 0.12 dex in [Fe/H], and 0.05 dex in [Ti/Fe]. Using this new calibration and the cleaned CARMENES spectra, we measure the $T_{\rm eff}$, [Fe/H], and [Ti/Fe] of the M dwarfs in our planet-hosting sample. The results are listed in Table 2.

3.2. A Bayesian Estimate of Stellar Ages

Starting with Bayes's theorem, the posterior probability distribution of a star's age, τ, given its titanium enhancement, [Ti/Fe], and our prior information, I, can be written as

$$p(\tau|[\mathrm{Ti/Fe}], I) \propto p(\tau|I)p([\mathrm{Ti/Fe}]|\tau, I). \quad (1)$$

Here the prior information includes three propositions: (1) a prior probability distribution for τ based on previous information, which in this case will be the star's peculiar velocities; (2) a model for the likelihood of a given [Ti/Fe] measurement as a function of age; and (3) that the measurement uncertainty in [Ti/Fe] can be described by a Gaussian with standard deviation $\sigma_{\rm [Ti/Fe]} = 0.05$ dex.

3.2.1. FGK Calibration Sample

In the following sections, we describe a data-driven approach to estimate the kinematic prior and [Ti/Fe] likelihood. For this approach, we require an unbiased sample of stars with known age, kinematics, and [Ti/Fe]. The Veyette et al. (2017) method to measure [Ti/Fe] was calibrated to match the Brewer et al. (2016, hereafter B16) catalog of detailed abundances for 1617 FGK stars. Therefore, to ensure consistency and reduce systematic errors, we used this same catalog to develop our kinematic–[Ti/Fe]—age model. To estimate the ages of the B16 stars, we used the isochrones package (Morton 2015) with the MIST stellar evolution models (Choi et al. 2016; Dotter 2016). We describe this process in detail in the Appendix.

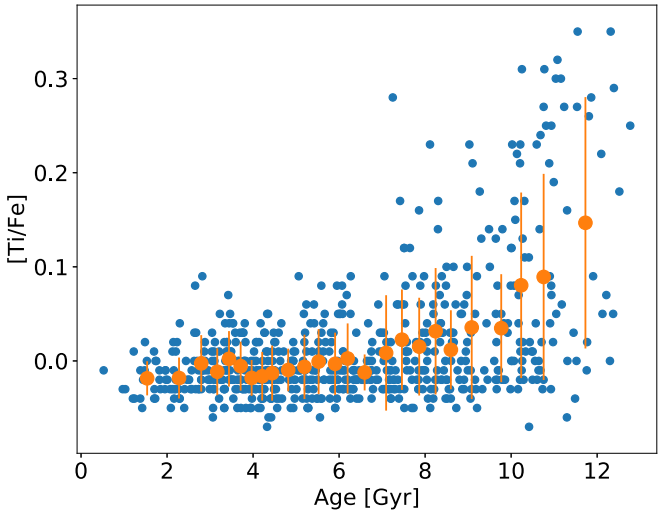

Figure 1. B16 [Ti/Fe] measurements of solar-neighborhood FGK stars vs. our stellar ages. Large orange circles denote the mean [Ti/Fe] in 25 age bins spaced so that each bin contains approximately the same number of stars. Error bars indicate the standard deviation in each bin.

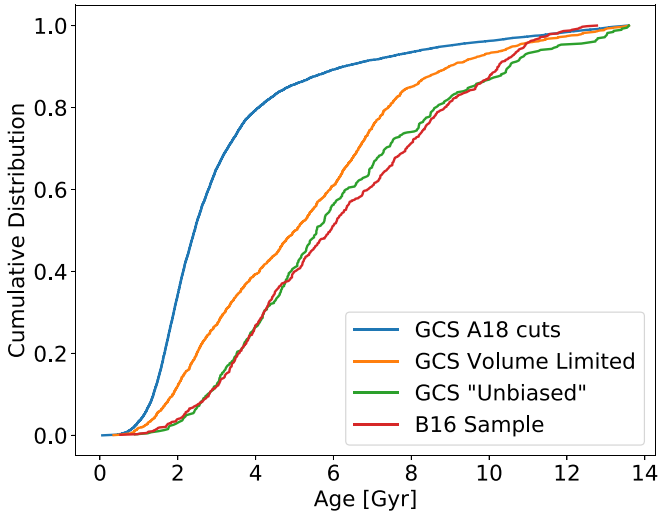

Figure 2. Cumulative distributions of ages in the GCS sample used by A18, a volume-limited sample of the GCS, an "unbiased" sample of the GCS, and our sample of B16 stars. See Section 3.2.2 for more information on each sample.

B16 fit for and removed from their abundance estimates any systematic trends with temperature; however, this trend was only assessed over a limited range of $T_{\rm eff}$ and log g. We found that systematic trends in [Ti/Fe] still existed for stars with $T_{\rm eff} > 6100$ K and log $g < 3.6$, so we excluded those stars from further analysis. We also excluded stars with best-fit A_V values >0.1. All stars in this sample are solar-neighborhood stars, and we do not expect significant extinction. These cuts, combined with the initial requirement that stars have a parallax measurement available in the literature and convergence criteria as described in the Appendix, leave 672 FGK stars for which we have reliable [Ti/Fe] and age estimates. Figure 1 shows the general trend of increasing [Ti/Fe] with increasing age.

Of these 672 stars, 658 have radial velocities and full five-parameter astrometric solutions in *Gaia* DR2 (Gaia Collaboration et al. 2018; Lindegren et al. 2018), which we used to calculate the U, V, and W peculiar velocities of each star (calculations based on code adapted from Rodriguez 2016).

3.2.2. Kinematic Prior

Almeida-Fernandes & Rocha-Pinto (2018, hereafter A18) introduced a method for estimating the age of a star based on its peculiar velocities alone. They modeled the components of the velocity ellipsoid of field stars as Gaussian distributions with age-dependant dispersion. They used the Geneva-Copenhagen Survey (GCS; Nordström et al. 2004; Casagrande et al. 2011) to fit for the dispersion of these distributions as functions of age, as well as the V component of the solar motion, $V_\odot'$, and the vertex deviation, ℓ_v. Evaluating the product of the three distributions at a given age produces the likelihood function for the measured U, V, and W velocities. We employ a prior probability distribution for a star's age based on the posterior probability distribution given by Equation (10) of A18 (method *UVW*),

$$p(\tau|U,\,V,\,W) \propto \prod_{i=1,2,3} \frac{1}{\sqrt{2\pi}\,\sigma_i(\tau)} \exp\left(-\frac{v_i^2}{2\sigma_i(\tau)^2}\right), \quad (2)$$

where v_1, v_2, and v_3 are the star's velocities in terms of the components of the velocity ellipsoid as defined by Equations (4)a–c of A18 and $\sigma_1(\tau)$, $\sigma_2(\tau)$, and $\sigma_3(\tau)$ are power laws with parameters from Table 1 of A18.

A18 made various cuts to the Casagrande et al. (2011) GCS catalog to ensure high-quality kinematic data and age estimates. The age distribution of their subsample is similar to the full, magnitude-limited GCS, which is known to be biased toward bright F-type stars (Nordström et al. 2004). Since the main-sequence lifetime of a 1.1 $M_\odot$ star is roughly half the age of the universe (Choi et al. 2016), using the full GCS significantly biases kinematic age estimates toward younger ages. In Figure 2, we show age cumulative distributions for the A18 sample compared to a volume-limited sample of the GCS ($d < 40$ pc). The volume-limited sample is significantly shifted toward older ages.

This volume-limited sample still contains a number of F dwarfs with main-sequence lifetimes much shorter than the age of the universe, which biases the sample against older stars. In an attempt to create a sample of stars that better matches the true age distribution of low-mass stars in the solar neighborhood, we further restrict the volume-limited sample to stars with $0.9\,M_\odot < M_\star < 1\,M_\odot$. This restricts the sample to mainly G dwarfs whose lifetimes are not significantly shorter than the age of the universe and for which the GCS is mostly complete out to 40 pc. The lower limit in mass excludes stars for which the ages are not well constrained. Figure 2 also shows the age distributions for this "unbiased" sample of the GCS and our sample of B16 stars. However, we note that it is extremely difficult to assemble a truly unbiased and complete sample of stars. The B16 sample is comprised of stars originally observed as part of the California Planet Survey (Howard et al. 2010), a

Table 3
Best-fit Constants for Equation (8)

		a	b	c
Comp. 1	Mean	-0.0160	1.65×10^{-7}	4.99
	Variance	3.19×10^{-4}	1.12×10^{-11}	7.51
	Weight	0.982	-6.78×10^{-4}	2.73
Comp. 2	Mean	-0.0116	8.55×10^{-4}	2.31
	Variance	3.44×10^{-4}	7.00×10^{-12}	8.13
	Weight	0.018	6.78×10^{-4}	2.73

radial velocity (RV) exoplanet survey. As such, it is biased against stars with excessive velocity jitter and faint stars. Our log g and $T_{\rm eff}$ cuts, along with our requirement that each star have Tycho-2 and 2MASS magnitudes as described in the Appendix, introduce additional biases. Overall, however, these biases do not result in any significant age bias for our final sample, as evidenced by the similarity between the age distributions for our B16 sample and the volume-limited "unbiased" GCS sample. This is largely a result of the fact that both samples have been limited to solar-neighborhood Sun-like stars. As these stars have lifetimes on the order of the age of the universe, their age distribution should be very similar to the age distribution of solar-neighborhood M dwarfs.

For consistency, we used our sample of B16 stars to recalibrate the A18 kinematic likelihood. We found the following best-fit relations for the vertex deviation, V component of the solar motion, and dispersion in the three components of the velocity ellipsoid as functions of time:

$$\ell_v = 0.406e^{-0.163\tau}, \tag{3}$$

$$V'_\odot = 0.314\tau^2 - 1.28\tau + 17.0, \tag{4}$$

$$\sigma_1 = 13.6\tau^{0.484}, \tag{5}$$

$$\sigma_2 = 7.32\tau^{0.493}, \tag{6}$$

$$\sigma_3 = 4.20\tau^{0.703}, \tag{7}$$

where all velocities are in km s^{-1}. We also calculate the U and W components of the solar motion to be 9.33 and 7.95 km s^{-1}, respectively.

We used proper motions and parallaxes from Gaidos et al. (2014) along with radial velocities from R18 to calculate the U, V, and W peculiar velocities for each M dwarf in our exoplanet-host sample. The velocities for each star are listed in Table 2. We used these velocities and Equations (3)–(7) to calculate the posterior probability distributions of the kinematic ages given by Equation (2). We used these posteriors as the prior probability in Equations (1).

3.2.3. A Data-driven [Ti/Fe] Likelihood

Following the approach of A18 for constructing a data-driven likelihood function, we used a sample of FGK stars with measured [Ti/Fe] and stellar ages to calculate the likelihood of a star's measured [Ti/Fe] given an assumed age.

We first divided our FGK sample into 25 age bins spaced so that each bin contains roughly an equal number of stars (~27 per bin). Motivated by the existence of two chemically distinct populations in the solar neighborhood (e.g., Fuhrmann 1998), we modeled the [Ti/Fe] distribution within a bin as a Gaussian mixture model with two components. We fit for the means, variances, and weights of each component via expectation maximization.[3] We assessed the uncertainty in the mixture model parameters by bootstrap resampling the [Ti/Fe] distribution within an age bin and refitting the mixture model, repeating this 10,000 times. In order to create a continuous likelihood as a function of age, we fit an offset power law of the form

$$\theta_i(\tau) = a + b\tau^c \tag{8}$$

to each mixture model parameter, θ_i. Here τ is the average age of the stars in the bin. We determined the best-fit parameters via χ^2 minimization and list them in Table 3. Figure 3 shows our mixture model parameters as a function of age, their uncertainties, and our power-law fits. Note that since the weights of the two components must sum to unity, we only fit to the weights of one component.

Figure 4 shows our Gaussian mixture distributions with means, variances, and weights given by Equation (8) with the best-fit parameters from Table 3. In order to use these distributions as likelihood functions for our planet-hosting M dwarf sample, we incorporate the uncertainty in our M dwarf

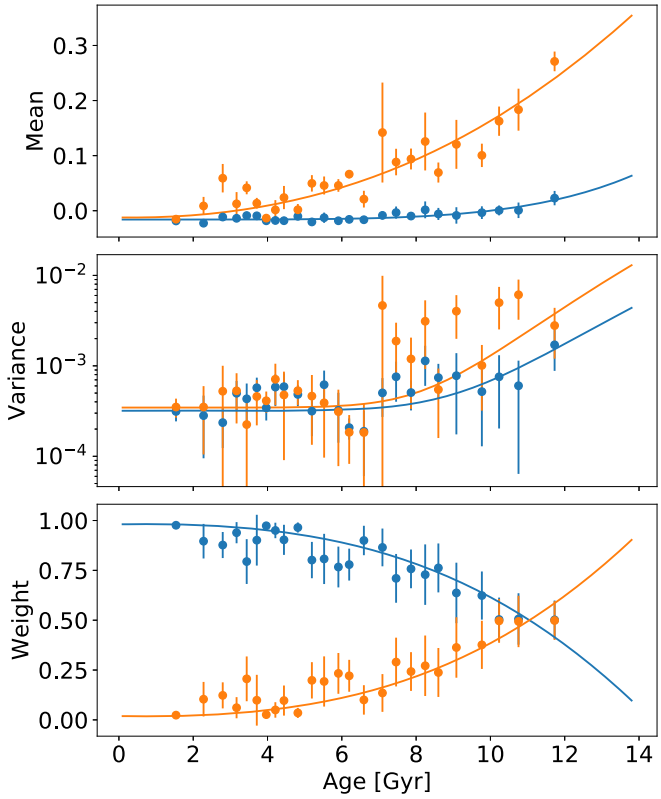

Figure 3. Means, variances, and weights of the two components (blue and orange) of our Gaussian mixture model as functions of age. Errors are from bootstrap resampling within each age bin. Solid lines are fits to the model parameters based on Equation (8) with the best-fit parameters from Table 3.

[3] Specifically, we used the Scikit-learn `GaussianMixture` package (Pedregosa et al. 2011).

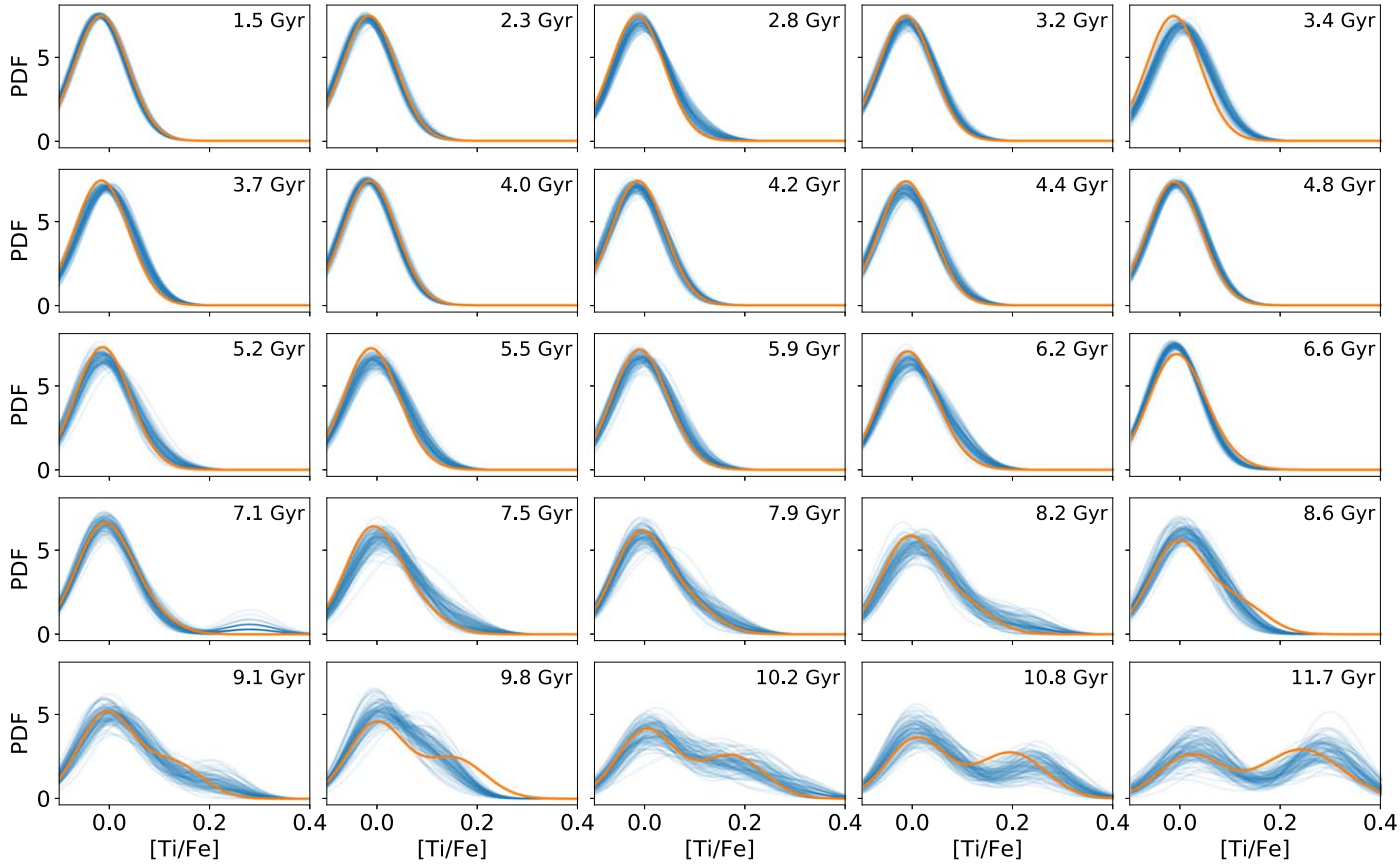

Figure 4. Comparison of the [Ti/Fe] distribution of the B16 sample within each age bin to our Gaussian mixture model. The average age of the bin is shown in the top right corner of each subplot. Semitransparent blue lines represent the KDE distributions from 100 bootstrap samplings of the B16 [Ti/Fe] distribution within each age bin. Orange lines represent our empirical likelihood function derived from Gaussian mixture models with parameters from our power-law fits (Equation (8)) with the best-fit parameters from Table 3). Note that they are not direct fits to the distributions in blue. To incorporate the uncertainty in our M dwarf [Ti/Fe] measurements, we have convolved our empirical likelihoods with a Gaussian kernel with a standard deviation of 0.05 dex. We also use a Gaussian kernel with a standard deviation of 0.05 dex in the KDEs.

[Ti/Fe] measurements by convolving the Gaussian mixture distributions with a Gaussian kernel with a standard deviation of 0.05 dex.[4] These distributions represent the empirical probability of measuring a given [Ti/Fe] for a given stellar age, incorporating both the intrinsic scatter in the [Ti/Fe]–age relation and the uncertainty in our M dwarf [Ti/Fe] measurements. The uncertainty in the B16 [Ti/Fe] measurements is much smaller than the intrinsic scatter within an age bin and is inherently included in this scatter. For qualitative comparison, we also show kernel density estimation (KDE) distributions from 100 bootstrap resamplings of the B16 [Ti/Fe] distribution within each age bin. We used a Gaussian kernel with a standard deviation of 0.05 dex. Evaluating the Gaussian mixture model at a measured [Ti/Fe] gives the likelihood as a function of age.

4. Results

Figure 5 shows the prior probability distribution, likelihoods, and posterior probability distribution for the age of each planet-hosting M dwarf in the CARMENES sample. Table 2 lists the median of the posterior and $\pm 1\sigma$ uncertainties corresponding to the 16th and 84th percentiles of the posterior.

[4] Thanks to the distributive property of convolution and the fact that all distributions are Gaussian, this is equivalent to simply adding 0.0025 dex of additional variance to each Gaussian component.

This approach preserves the astrophysical scatter in the relation between [Ti/Fe] and age, whereas fitting a parametric model directly to the [Ti/Fe]–age relation would assume all scatter is due to measurement uncertainty and underestimate the uncertainty in predicted ages. However, this also means that our age uncertainties may be overestimated, as all scatter is taken to be astrophysical even though there is certainly measurement error (and likely systematic error) in both the [Ti/Fe] and age estimates. Nevertheless, we take the conservative approach of assuming all scatter is astrophysical and carry it through to our final age posteriors.

5. Discussion

Taken as an ensemble, we find that exoplanets orbit M dwarfs with a range of ages typical for the solar neighborhood. Our median age estimates range from 4 to 9 Gyr. Figure 6 shows the eccentricities of all planets in our sample compared with the age of the host star. The sample is too small to draw any significant conclusions about the eccentricity distribution as a function of age. However, we do find that there are a number of single planets on short-period orbits with low but nonzero eccentricities ($e \sim 0.1$–0.3) at all ages. We also find that, on average, the sample is slightly Ti-enhanced. The mean [Ti/Fe] is 0.033 ± 0.015 dex, and most M dwarfs in the sample have [Ti/Fe] > 0. However, most are within their measurement error (0.05 dex) of the solar value, and only one,

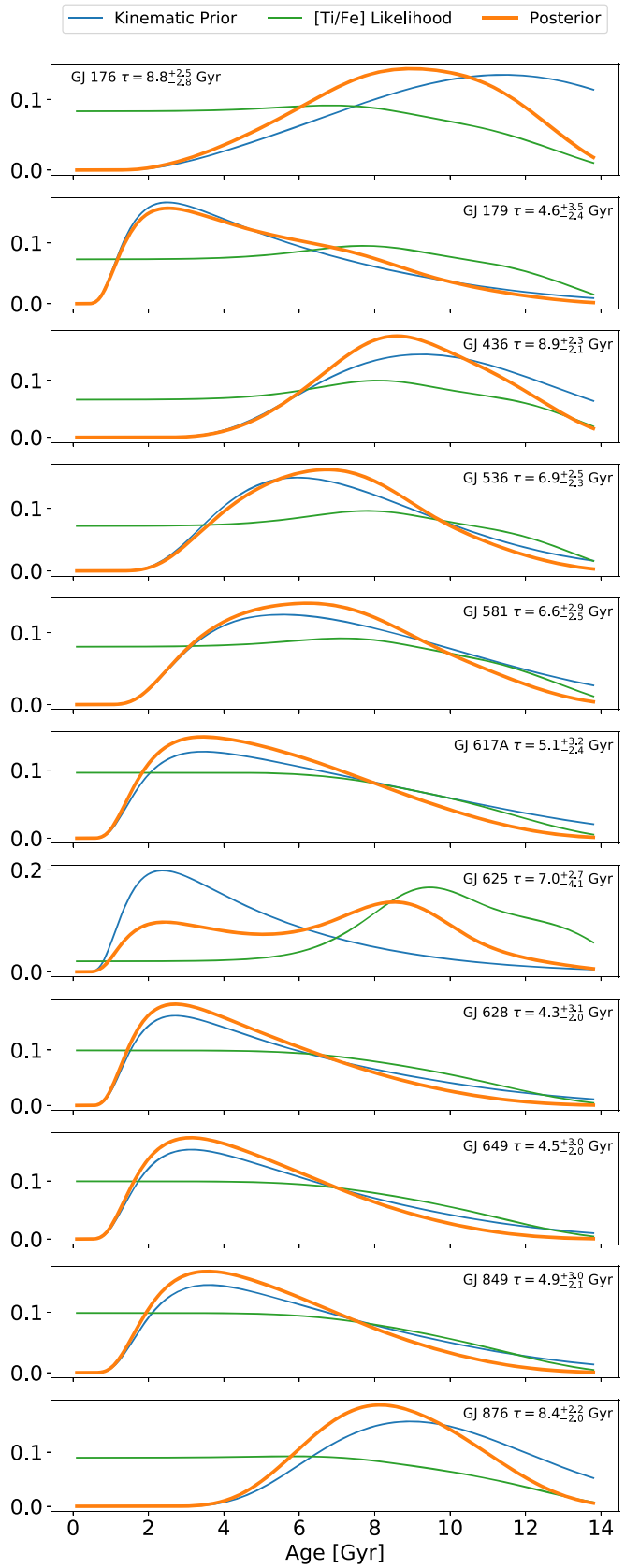

Figure 5. Prior probability distribution, likelihoods, and posterior probability distribution for the age of each planet-hosting M dwarf in the CARMENES sample. Median and $\pm 1\sigma$ age estimates are listed in Table 2.

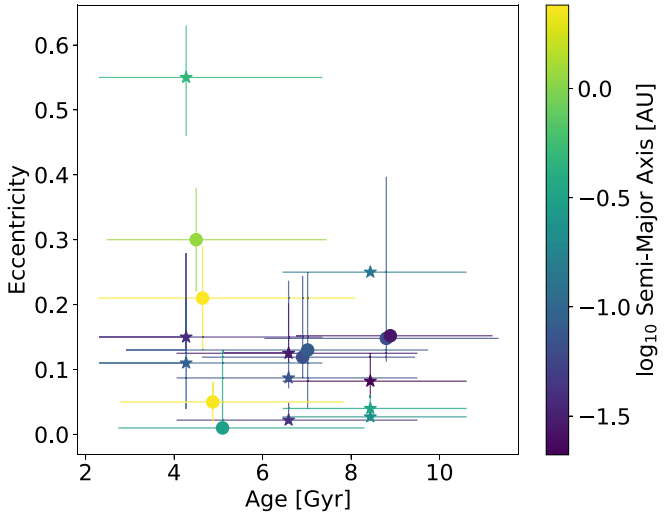

Figure 6. Planet eccentricity as a function of stellar age, colored by semimajor axis. Planets in multi-planet systems are denoted as stars.

GJ 625, has the distinct chemical signature of the metal-poor, α-rich thick disk.

5.1. Tidal Damping and Migration

In the absence of interactions with a third body, tides raised on both the planet and star are expected to damp out eccentricities and reduce the semimajor axis for planets orbiting within $\sim$0.2 au of their host star (Goldreich & Soter 1966). Tidal circularization likely explains the observed lack of highly eccentric ($e > 0.5$) planets on close-in orbits noted in numerous studies (e.g., Rasio & Ford 1996; Kane et al. 2012; Kipping 2013). One way to determine whether or not a planet is currently undergoing tidal damping and migration is to estimate its tidal circularization timescale, $\tau_{\rm circ}$ (Equation (4) of Jackson et al. 2008). However, as Jackson et al. (2008) pointed out, tidal effects fall off rapidly with increasing semimajor axis. Therefore, it is important to model the coupled evolution of both eccentricity and semimajor axis to calculate the true time it takes to circularize an orbit.

5.1.1. Simplified Tidal Circularization Timescales

For illustrative purposes, we used Equation (4) in Jackson et al. (2008; including the corrected numerical coefficient from Jackson et al. 2009) to calculate the simplified tidal circularization timescales for the planets in our sample. Calculating the tidal circularization timescale requires assuming a value for the tidal dissipation parameter Q, a unitless quality factor that is inversely proportional to tidal dissipation —smaller Q results in stronger dissipation. We assumed a tidal dissipation parameter for the star of $Q_\star = 10^{5.5}$ and for the planet of $Q_{\rm p} = 10^{6.5}$, as suggested by Jackson et al. (2008), although we note that the tidal $Q_{\rm p}$ is no doubt different for each planet and likely depends on each planet's mass and structure. In our calculations, we used the planetary masses, semimajor axes, and eccentricities in Table 1. For planetary radii, we used the empirical mass–radius–incident flux relation of Weiss et al. (2013, Equations (8) and (9)). In one case, GJ 436 b, we had a measurement of the planetary radius from transit observations

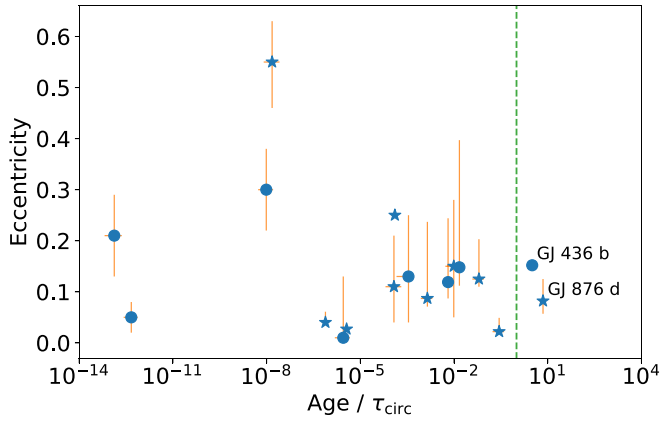

Figure 7. Age divided by the simplified tidal circulation timescale, assuming $Q_p = 10^{6.5}$, vs. eccentricity. A green line indicates where age $= \tau_{circ}$. Most planets in our sample have very long tidal circulation timescales, such that tides are not expected to play a large role in the evolution of the planet even over the lifetime of the universe. Only two planets (labeled) have ages longer than their circularization timescales.

(Maciejewski et al. 2014). We estimated stellar masses and radii from the empirical absolute *K*-band magnitude relations of Benedict et al. (2016, Equation (11) with coefficients from Table 13) and Mann et al. (2015, Equation (5) with coefficients from Table 1),[5] respectively. For both relations, we used *K*-band magnitudes from 2MASS (Skrutskie et al. 2006) and parallaxes from *Gaia* DR1 (Gaia Collaboration et al. 2016b, 2016a; Lindegren et al. 2016). We accounted for the *Gaia* zero-point offset; however, it has little effect, as our stars are all nearby with parallaxes of order 100 mas.

Figure 7 shows the eccentricities of the planets in our sample versus the host-star age divided by the tidal circularization timescale. Most planets in our sample have very long timescales, such that it is unlikely that they underwent recent tidal evolution. Two planets, GJ 436 b and GJ 876 d, have tidal circularization timescales shorter than the age of their host star. It has been suggested that GJ 436 b has a massive unseen companion that maintains its moderate eccentricity via Kozai interactions (Beust et al. 2012), so its short tidal circularization timescale may not be so surprising. GJ 876 d has three outer companions that are in a Laplace resonance (Rivera et al. 2010). The innermost planet in the system, GJ 876 d, is not expected to interact with the outer three planets (Trifonov et al. 2018), so its nonzero eccentricity is surprising given its short circularization timescale. We discuss GJ 436 b and GJ 876 d further in Sections 5.2.3 and 5.2.11, respectively.

5.1.2. Minimum Q_p

As pointed out by Jackson et al. (2008), the simplified tidal circularization timescale ignores the coupled evolution of eccentricity and semimajor axis and can underestimate the true time to circularize. An alternative approach is to numerically integrate back the tidal evolution equations for both eccentricity and semimajor axis (Equations (1) and (2) of Jackson et al. 2009) from the current age of the star to its formation. Doing so results in the initial eccentricity and semimajor axis of the planet's orbit just after the protoplanetary disk dissipated, assuming no interactions with other bodies in the system. Since we have a posterior for the age of the star, we can determine the probability distribution for the initial eccentricity and semimajor axis of a planet if we assume a Q_p and $Q_\star$. To do so, we integrate back the tidal evolution equations 10,000 times, each time drawing a random age from our age posteriors. We show an example of this for GJ 876 d in Figures 8 and 9, where we assume $Q_\star = 10^{5.5}$ and $Q_p = 10^{6.5}$ and $10^{5.5}$, respectively. Assuming a Q_p of $10^{6.5}$ results in a median initial eccentricity and semimajor axis of $e_i = 0.7$ and $a_i = 0.035$ au. However, if we assume a Q_p of only $10^{5.5}$, the median initial eccentricity exceeds 1. Therefore, we can constrain the Q_p of GJ 876 d to be greater than $\sim 10^{5.5}$.

Following this approach, we can use our host-star ages to estimate the minimum Q_p possible for each planet by stepping through possible Q_p values until the initial eccentricity exceeds 1. For each planet, we estimate the initial eccentricity probability distribution for 100 Q_p values spaced logarithmically from 10 to 10^7. We take the maximum Q_p at which the median initial eccentricity is greater than 1 as the minimum possible Q_p for the planet. We hold the stellar tidal dissipation parameter fixed at $10^{5.5}$. For planets that are susceptible to tidal

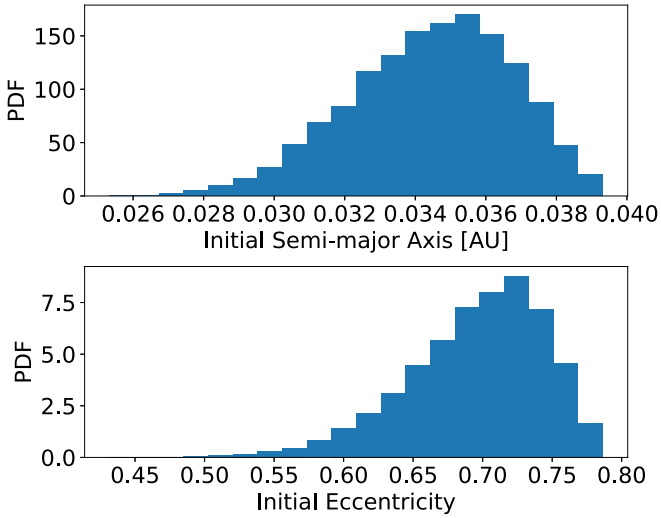

Figure 8. Probability distributions for the initial eccentricity and semimajor axis of GJ 876 d based on integrating back the tidal evolution equations of Jackson et al. (2009) with current ages drawn from our age posterior. Here we assume $Q_\star = 10^{5.5}$ and $Q_p = 10^{6.5}$.

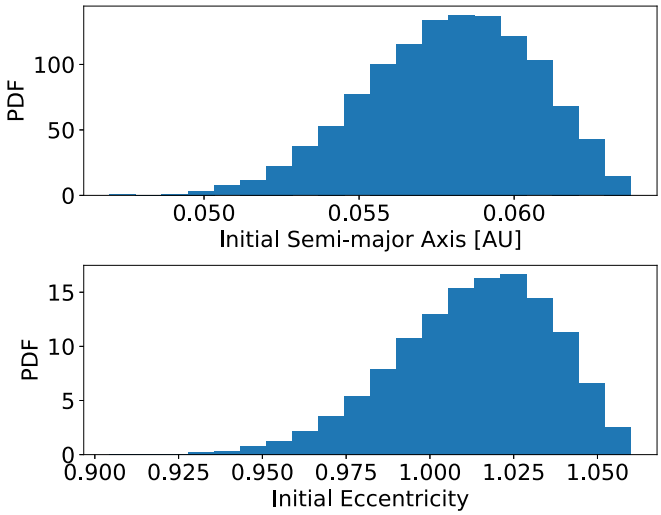

Figure 9. Same as Figure 8 but with $Q_\star = 10^{5.5}$ and $Q_p = 10^{5.5}$.

[5] We used the values from Table 1 of the erratum (Mann et al. 2016).

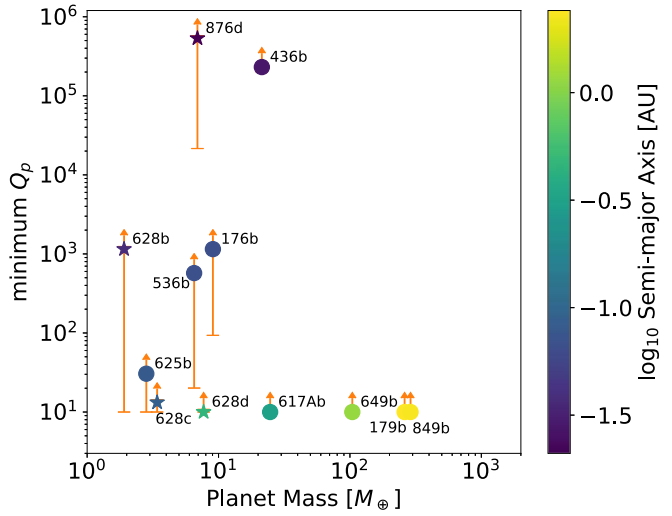

Figure 10. Minimum Q_p vs. planet mass, colored by orbital period. Stars indicate planets in multi-planet systems. Lower error bars are calculated by assuming the planet radius and eccentricity are overestimated by 1σ. Planets known to be gravitationally interacting with other planets in the system have been excluded (GJ 581 b, c, e and GJ 876 b, c, e).

effects around M dwarfs (i.e., on close-in orbits), the effect of the stellar tide is negligible. The minimum Q_p values are shown in Figure 10. Again, this assumes only tidal interactions with the host star, so the results are not necessarily meaningful for dynamically interacting multi-planet systems. We have excluded from the figure planets known to be gravitationally interacting with a companion (GJ 581 b, c, e and GJ 876 b, c, e). To assess the sensitivity of our minimum Q_p estimates to measurement uncertainties, we redid the analysis using planet radii and eccentricities that were smaller by 1σ. For radii, we used the RMSE of the mass–radius relation ($1.41\,R_\oplus$ for $M < 150\,M_\oplus$, $1.15\,R_\oplus$ for $M \geqslant 150\,M_\oplus$; Weiss et al. 2013), except for GJ 436 b, where we used the radius uncertainty quoted by Maciejewski et al. (2014). For eccentricities, we used the lower uncertainties listed in Table 1.

The tidal dissipation parameter Q_p is poorly constrained even for the planets in the solar system. Gas giants like Jupiter and Saturn have Q_p values somewhere around 10^5–10^6 (Goldreich & Soter 1966; Ioannou & Lindzen 1993; Ogilvie & Lin 2004). However, Lainey et al. (2009, 2012, 2017) suggested that Jupiter's and Saturn's tidal Q_p are much lower, around 35,000 and 2500, respectively. Neptune and Uranus both have Q_p values around 10^4 (Goldreich & Soter 1966; Zhang & Hamilton 2008). Rocky planets have low Q_p values around 10–200 (Goldreich & Soter 1966; Murray & Dermott 2000; Lainey et al. 2007; Henning et al. 2009). Because of the large separation between gas giant and terrestrial Q_p values, they can be used to differentiate between rocky and gaseous planets (Barnes 2015). Since we can only provide a lower bound on Q_p, we cannot place strict constraints on the composition of these planets, though a high minimum Q_p might suggest that the planet is more like a gas giant than a rocky planet. It is also important to note that tidal evolution is strongly dependent on the radius of the planet ($1/\tau_{\rm circ} \propto R_p^5$). For all but one planet, we assume a radius based on mass and incident flux. Therefore, a high minimum Q_p does not necessarily rule out a rocky composition. Rather, a high minimum Q_p indicates that a planet could be affected by tidal interactions, if its true Q_p is not well above our lower limit and its true radius is not much less than that inferred from empirical mass–radius relations, which are know to have significant scatter (Wolfgang & Lopez 2015; Wolfgang et al. 2016). A small minimum Q_p simply means the planet is insensitive to tidal effects on timescales of the stellar lifetime, e.g., if it obits at a large semimajor axis.

It is also important to note that the tidal evolution equations are only valid under the assumption that the planet's orbital period is shorter than the star's rotational period. While this may not be valid for all systems in this study, it is valid for the most interesting systems, those with short-period planets ($P < 10$ days) around old stars. Field early-to-mid-M dwarfs typically have rotation periods >10 days (McQuillan et al. 2013), and kinematically old mid-M dwarfs typically rotate with periods >70 days (Irwin et al. 2011; Newton et al. 2016).

5.2. Individual Systems

In the following, we discuss individual systems in more detail.

5.2.1. GJ 176

GJ 176 hosts a super-Earth in an 8.8 day orbit originally discovered by Forveille et al. (2009). Trifonov et al. (2018) published updated parameters for GJ 176 b, incorporating 23 new CARMENES observations and confirming an $M \sin i \approx 9 M_\oplus$ planet in an ~8.8 day orbit. They reported a mildly eccentric orbit with $e = 0.148^{+0.249}_{-0.036}$.

Eggen (1998) proposed that GJ 176 is a member of the moving group HR 1614 based on its kinematics. Feltzing & Holmberg (2000) estimated HR 1614 to be about 2 Gyr old. However, our analysis suggests that GJ 176 is an older star with an age of $8.8^{+2.5}_{-2.8}$ Gyr and rules out ages less than 2 Gyr at the 3σ level. Furthermore, De Silva et al. (2007) spectroscopically analyzed 18 proposed members of HR 1614 and found the cluster to be metal-rich with $\log \varepsilon_{\rm Fe} = 7.77 \pm 0.033$ dex. De Silva et al. (2007) also found that four out of the 18 stars they studied had lower metallicities with $\log \varepsilon_{\rm Fe} = 7.44$–$7.55$ dex and deviated from the cluster mean abundances in all elements except the *n*-capture elements, suggesting that they are not members of HR 1614. We measure an iron abundance for GJ 176 of only $\log \varepsilon_{\rm Fe} = 7.5 \pm 0.1$ dex, further suggesting that it is not a member of HR 1614.

GJ 176 b has the second-highest minimum Q_p (~10^3) of all single-planet systems in our sample. At a minimum mass of $\sim 9\,M_\oplus$, GJ 176 b is likely more similar to Uranus and Neptune than to a massive, rocky super-Earth. This is supported by our minimum Q_p for GJ 176 b, which is close to the Q_p of Uranus and Neptune. Orbiting at only 0.066 au, GJ 176 b has likely undergone some tidal evolution. Assuming a radius of $3.5\,R_\oplus$ and a Q_p of 10^4, we estimate that GJ 176 b started with a high initial eccentricity of $e_i \approx 0.7$ and migrated in from an initial semimajor axis of $a_i \approx 0.1$ au.

5.2.2. GJ 179

GJ 179 is one of the few M dwarfs known to host a Jupiter analog. GJ 179 b is a Jupiter-mass planet ($M \sin i = 0.82 M_{\rm Jup}$) in a slightly eccentric ($e = 0.21 \pm 0.08$) 6.3 yr orbit (Howard et al. 2010). Despite a slight Ti enhancement, the kinematics of GJ 179 suggest a moderate age of $4.6^{+3.5}_{-2.4}$ Gyr but with a long tail of probability up to older ages.

Orbiting at such a large distance from its host star, GJ 179 b is not expected to be affected by tidal interactions with the host star.

5.2.3. GJ 436

GJ 436 was the second M dwarf found to host an exoplanet (Butler et al. 2004). GJ 436 b has roughly the same radius, mass, and density as Neptune but orbits with a period of only 2.6 days (Maciejewski et al. 2014). Butler et al. (2004) originally estimated that GJ 436 is more than 3 Gyr old based on its kinematics and chromospheric activity. By combining kinematics with Ti enhancement, we constrain the age to be $8.9^{+2.3}_{-2.1}$ Gyr, making GJ 436 the oldest planet host in our sample (with the potential exception of GJ 625; see Section 5.2.7).

The old age of GJ 436 is surprising considering that it hosts a short-period planet in an eccentric orbit ($e = 0.152 \pm 0.009$; Trifonov et al. 2018). Bourrier et al. (2018) recently reported that the orbit of GJ 436 b is not only eccentric but also nearly perpendicular with the spin axis of the star.

One scenario that has been proposed to explain the eccentricity of GJ 346 b is interaction with a third body (Demory et al. 2007; Maness et al. 2007; Mardling 2008; Ribas et al. 2008). Tong & Zhou (2009) investigated the possible locations of a dynamical companion in either a resonant or nonresonant orbit and argued that the eccentricity of GJ 436 b cannot be maintained by either a nearby or distant companion. Batygin et al. (2009) confirmed that, for most scenarios, the presence of a second planet does not keep GJ 436 b from rapidly circularizing. However, they found that under certain initial conditions where the eccentricities of the two planets are locked at a quasi-stationary point, the eccentricity damping of GJ 436 b can be extended to ∼8 Gyr.

Beust et al. (2012) put forward another hypothesis, suggesting that GJ 436 b originally orbited at a larger semimajor axis and migrated to its current orbit via Kozai migration induced by a distant perturber. In this scenario, the eccentricity damping of GJ 436 b can be delayed by several Gyr. Bourrier et al. (2018) estimated the age of GJ 436 to be ∼5 Gyr based on its rotation period of 44 days and found that Kozai migration could explain both the eccentricity and obliquity of GJ 436 b.

Morley et al. (2017) found that additional interior heat from tidal dissipation is required to explain the observed thermal emission of GJ 436 b. They were able to constrain the tidal Q_p of GJ 436 b to 2×10^5–10^6. This agrees well with our minimum Q_p estimate of $\sim 10^5$. With a $Q_p > 10^5$, the tidal dissipation is weak enough that an unseen third body is not required to explain the nonzero eccentricity. However, it does mean that the orbit of GJ 436 b has been significantly altered by tidal effects over its lifetime. Assuming a $Q_p = 10^6$, GJ 436 b would have initially orbited with an eccentricity around ∼0.8 at a distance of ∼0.05 au. However, this scenario does not explain the high obliquity of the current orbit reported by Bourrier et al. (2018).

5.2.4. GJ 536

GJ 536 hosts a super-Earth planet in an 8.7 day orbit (Suárez Mascareño et al. 2017a). Using additional RV data from the CARMENES survey, Trifonov et al. (2018) refined GJ 536 b's mass estimate to $M \sin i = 6.52^{+0.69}_{-0.40} M_\oplus$ and the eccentricity of the orbit to $e = 0.119^{+0.125}_{0.032}$. We estimate the age of GJ 536 to be $6.9^{+2.5}_{-2.3}$ Gyr.

GJ 536 b is very similar to GJ 176 b. Both orbit at ∼0.066 au with similar eccentricities, 0.15 and 0.12. GJ 176 b has a slightly higher minimum mass than GJ 536 b, 9 $M_\oplus$ versus 6.5 $M_\oplus$. We estimate the minimum Q_p of both planets to be $\sim 10^3$. In the absence of interactions with other unseen planets in the system, GJ 176 b and GJ 536 b are likely similar mini-Neptune planets with extensive gaseous atmospheres. Both are also likely to have undergone tidal circularization and migration. Assuming a Q_p of 10^4, we estimate that GJ 536 b initially orbited at ∼0.08 au with an eccentricity of ∼0.5.

5.2.5. GJ 581

GJ 581 hosts three bona fide planets: GJ 581 b (Bonfils et al. 2005b), GJ 581 c (Udry et al. 2007), and GJ 581 e (Mayor et al. 2009). The three planets orbit in a very compact configuration with semimajor axes between 0.029 and 0.074 au. Trifonov et al. (2018) used an *N*-body model to show that all three planets are dynamically interacting and in a stable configuration where each planet's semimajor axis is constant but their eccentricities oscillate on timescales of 50 and 500 yr. Since all three planets are interacting, our minimum Q_p estimates are invalid. Trifonov et al. (2018) showed that this configuration is stable for at least 10 Myr. Our age estimate for GJ 581 of $6.6^{+2.9}_{-2.5}$ Gyr suggests that these compact, interacting systems can be stable for several Gyr. This is further supported by the apparent ubiquity of these "compact multiples" (Muirhead et al. 2015).

5.2.6. GJ 617 A

HD 147379 (GJ 617 A) was the first star discovered to host a planet by the CARMENES survey (Reiners et al. 2018a). GJ 617 A b has a minimum mass of $M_p \sin i \sim 25 M_\oplus$ and orbits in a nearly circular ∼0.3 au orbit. As such, GJ 617 A b is unlikely to be strongly affected by tidal interactions with its host star.

Vican (2012) estimated the age of GJ 617 A to be ∼1 Gyr based on chromospheric activity and X-ray flux. However, they used the activity–age relations of Mamajek & Hillenbrand (2008), which were only calibrated down to early-K dwarfs ($B - V < 0.9$ mag), and GJ 617 A is a late-K/early-M with $B - V = 1.34$. We estimate a slightly older chemo-kinematic age for GJ 617 A of $5.1^{+3.2}_{-2.4}$ Gyr.

Reiners et al. (2018a) found an additional peak in the periodogram of GJ 617 A corresponding to a period of 21 days, which they attributed to the rotation period of the star. Pepper (2018) confirmed a 22 day rotation period based on 3304 KELT observations (Pepper et al. 2007). Agüeros et al. (2018) recently measured rotation periods for 12 K and M dwarfs in the 1.34 Gyr old cluster NGC 752. They found that late-K dwarfs similar in mass to GJ 617 A rotate with a rotation period of ∼15 days. Assuming a simple Skumanich-like evolution ($\tau \propto p_{\rm rot}^2$), a rotation period of 22 days for GJ 617 A would suggest an age of ∼3 Gyr, in rough agreement with our chemo-kinematic estimate.

5.2.7. GJ 625

GJ 625 was only recently discovered to host a super-Earth orbiting at the inner edge of the habitable zone (Suárez Mascareño et al. 2017b). A rocky planet orbiting at such a close

distance to its host star is expected to circularize on very short timescales. Indeed, the eccentricity of GJ 625 b is consistent with zero: $e = 0.13^{+0.12}_{-0.09}$. GJ 625 b is not likely to be currently undergoing tidal migration, although it may have in the past.

GJ 625 is a peculiar case where its kinematics strongly favor a young age; however, its low [Fe/H] and high [Ti/Fe] abundances are similar to older thick-disk members. This leads to a combined age posterior that is bimodal and has a significant probability at essentially all ages. The median and $\pm 1\sigma$ values of the posterior are $7.0^{+2.7}_{-4.1}$ Gyr. Estimating the age from the kinematic prior alone yields $3.9^{+3.3}_{-1.9}$ Gyr, whereas ignoring the kinematic prior and assuming a flat prior results in an age estimate from [Ti/Fe] alone of $9.5^{+2.5}_{-3.0}$ Gyr.

We can turn to other indications of an M dwarf's age to argue in favor of either the young or old interpretation of the age of GJ 625. A common indicator for the rough age of an M dwarf is its rotation period. Suárez Mascareño et al. (2017b) estimated the rotation period of GJ 625 to be $P = 77.8 \pm 5.5$ days. The relation between rotation period and age for M dwarfs is not well understood. However, studies of young open clusters and field M dwarfs suggest that M dwarfs, like solar-type stars, spin down over time as magnetized stellar winds carry away angular momentum (Irwin et al. 2007, 2011; McQuillan et al. 2013; Newton et al. 2016; Douglas et al. 2017; Rebull et al. 2017). Newton et al. (2016) found that field mid-M dwarfs like GJ 625 show a bimodal distribution in rotation period with peaks at ∼1 and ∼100 days. The evolutionary link between these two populations is not clear; however, Newton et al. (2016) found that M dwarfs with rotation periods >70 days are kinematically consistent with an old population with an average age of 5 Gyr. GJ 625's slow ∼80 day rotation is similar to that of the slowest rotating (and presumably oldest) stars in the field of similar mass (Newton et al. 2017) and is therefore more consistent with the older peak of our age posterior.

Montes et al. (2001) listed GJ 625 as a possible member of the young Ursa Major moving group, which would imply an age of only ∼0.5 Gyr (although Montes et al. 2001 did list it with the caveat that it fails both their peculiar velocity and radial velocity criteria). We can rule out membership based on GJ 625's long rotation period, low activity ($\log_{10}(R'_{HK}) = -5.5 \pm 0.2$; Suárez Mascareño et al. 2017b), and chemical dissimilarity (Tabernero et al. 2017). We also note that the BANYAN Σ web tool[6] lists a 0% probability that GJ 625 is a member of the Ursa Major moving group and a 99.9% probability that it is a field star (Gagné et al. 2018).

5.2.8. GJ 628

Wright et al. (2016) used archival HARPS spectra to discover three potentially rocky planets around GJ 628 (Wolf 1061), with one planet, GJ 628 c, orbiting within the habitable zone. Astudillo-Defru et al. (2017) ruled out a third planet orbiting at 67 days as originally proposed by Wright et al. (2016) but found significant evidence for a third planet orbiting at 217 days.

GJ 628 is one of a couple cases where a solar [Ti/Fe] estimate results in a very broad likelihood and the posterior is dominated by the kinematic prior that favors younger ages. Based on this, we estimate an age for GJ 628 of $4.3^{+3.1}_{-2.0}$ Gyr. However, Astudillo-Defru et al. (2017) claimed a rotation period of 95 days for GJ 628, which is supported by the photometric monitoring presented in Kane et al. (2017). Such a long rotation period suggests an age >5 Gyr, as discussed in the previous section. If a strict gyrochronological relation does exist for M dwarfs, this long rotation period is inconsistent with our age estimate.

We estimate a minimum $Q_p \sim 10^3$ for the innermost planet, GJ 628 b. Such a high minimum Q_p would suggest that the $M_p \sin i \sim 2M_\oplus$ planet is not rocky but in fact has a large gaseous envelope. However, GJ 628 b and GJ 628 c have eccentricities that are consistent with zero within the measurement error. If we assume their radii and eccentricities are overestimated by 1σ, we can no longer constrain the minimum Q_p to be greater than 10. Therefore, given that they are both likely rocky and orbit within 0.1 au of their host star, they likely were tidally circularized not long after their primordial disk dissipated.

Montes et al. (2001) listed GJ 628 as a member of the young (125 Myr; Stauffer et al. 1998) Pleiades moving group. However, the BANYAN Σ web tool lists a 0% probability that GJ 628 is a member of the Pleiades moving group and a 99.9% probability that it is a field star.

5.2.9. GJ 649

GJ 649 hosts one known planet with a minimum mass similar to Saturn, $M_p \sin i \sim 100M_\oplus$ (Johnson et al. 2010b). With a semimajor axis of 1.1 au, the orbit of GJ 649 b is not expected to be influenced by tidal effects.

GJ 649 is another case where a near-solar [Ti/Fe] does little to constrain the age of the star—other than ruling out the oldest ages—and the kinematics favor younger ages. We estimate an age of $4.5^{+3.0}_{-2.0}$ Gyr for GJ 649.

5.2.10. GJ 849

GJ 849 hosts a roughly Jupiter-mass planet in a nearly circular, ∼5 yr orbit (Butler et al. 2006). Orbiting at over 2 au, GJ 849 b is not expected to undergo any tidal circularization or migration. Butler et al. (2006) noted a linear trend in their RV time-series data, suggesting a possible second planet in the system on an even longer orbit. With RV measurements spanning 17 yr, Feng et al. (2015) found strong evidence for a second planet with $M \sin i \approx M_J$ orbiting with a period of 15.1 ± 1.1 yr.

Like GJ 628 and GJ 649, GJ 849 has nearly solar [Ti/Fe] and kinematics that skew the age posterior to younger ages. Based on this, we estimate the age of GJ 849 to be $4.9^{+3.0}_{-2.1}$ Gyr.

5.2.11. GJ 876

The planetary system around GJ 876 is a benchmark system for studying the formation and migration of planets in compact systems. GJ 876 hosts a total of four known planets, three of which are in a Laplace 1:2:4 mean-motion resonance (Rivera et al. 2010). The resonance is chaotic but expected to be stable on timescales of at least 1 Gyr (Rivera et al. 2010; Martí et al. 2013). The old age we infer for GJ 876 ($8.4^{+2.2}_{-2.0}$ Gyr) suggests that such chaotic resonances can be stable for several Gyr, assuming the planets migrated into this configuration soon after their formation (Batygin et al. 2015).

Even though the innermost planet, GJ 876 d, is not in the resonant chain with the other three planets, our old age for GJ 876 has some interesting implications for its past migration. Originally, Rivera et al. (2010) estimated that planet d orbited

[6] http://www.exoplanetes.umontreal.ca/banyan/banyansigma.php

with an unusually high eccentricity ($e = 0.207 \pm 0.055$) for a planet that orbits at only 0.02 au with a period of about 2 days. Recently, Millholland et al. (2018) and Trifonov et al. (2018) reanalyzed the system by fitting dynamical *N*-body models to existing and new RV data. Both analyses revised the eccentricity of planet d down to values more consistent with a circular orbit. Trifonov et al. (2018) reported a best-fit eccentricity of $e = 0.082^{+0.043}_{-0.025}$, while Millholland et al. (2018) reported a best-fit eccentricity of $e = 0.057 \pm 0.039$. Using the Trifonov et al. (2018) estimate for the eccentricity, we constrain the minimum Q_p of GJ 876 d to be $>5 \times 10^5$. Such a high Q_p is surprising for an $\sim 7\ M_\oplus$ planet. Our minimum Q_p for GJ 876 d is an order of magnitude higher than the Q_p of Uranus and Neptune and three orders of magnitude greater than the Q_p of terrestrial bodies.

A few scenarios could explain the nonzero eccentricity of GJ 876 d. One explanation is that the planet has a peculiar structure that is very inefficient at dissipating tidal energy. Another explanation is that GJ 876 d originally orbited with a larger semimajor axis where it gravitationally interacted with the outer three planets and, at some point in its history, fell out of a chaotic resonance with the outer planets and migrated in. A third scenario is that there is another, unseen planet in the system that is gravitationally interacting with GJ 876 d.

We note that the eccentricity of GJ 876 d has undergone downward revision recently. If additional observations in future studies lead to further downward revision and the conclusion that the orbit is essentially circular, it may not be necessary to invoke one of the above scenarios to explain the orbit of GJ 876 d. In that case, our minimum Q_p will be overestimated. However, given its proximity to its host star and our age estimate of $8.4^{+2.2}_{-2.0}$ Gyr for the system, GJ 876 d likely has undergone significant tidal circularization and migration in its lifetime.

Montes et al. (2001) listed GJ 876 as a member of the young Pleiades moving group, which is inconsistent with our old age estimate for the star. The BANYAN Σ web tool gives a 0% probability that GJ 876 is a member of the Pleiades moving group and an 81.7% probability that it is a field star. Interestingly, it also gives an 18.3% probability that GJ 876 is a member of the Beta Pictoris moving group.

6. Summary

We used a sample of well-studied FGK stars to develop a data-driven approach to estimate the ages of field stars from their composition and kinematics within a Bayesian framework. Our method relies on astrophysical trends between stellar ages, *UVW* space velocities, and titanium enhancement [Ti/Fe]. We applied our method to 11 exoplanet-hosting M dwarfs, making use of recent advancements in the detailed chemical analysis of M dwarfs (Veyette et al. 2016, 2017). We list our exoplanet-host ages in Table 2.

Tidal effects are expected to circularize the orbits of short-period planets around M dwarfs. However, we find that a number of close-in planets ($a < 0.1$ au) with mildly eccentric orbits ($e \sim 0.1$) in fact orbit relatively old stars with ages around 8 Gyr. For these stars, we can constrain the minimum tidal Q_p possible that can explain the current eccentricity, semimajor axis, and age of the system.

We find that GJ 176 b and GJ 536 b, two short-period mini-Neptune planets on similar orbits, have similar minimum Q_p values of $\sim 10^3$, suggesting that mini-Neptune planets have Q_p values closer to those of the ice giants than the terrestrial planets in our solar system. We estimate the ages of the host stars of these systems to be $8.8^{+2.5}_{-2.8}$ and $6.9^{+2.5}_{-2.3}$ Gyr and find that both planets likely have undergone tidal migration and circularization and initially orbited farther from their host star with eccentricities >0.5.

We estimate an age of $8.9^{+2.3}_{-2.1}$ Gyr and a minimum Q_p of $\sim 10^5$ for GJ 436 b. Our Q_p limit agrees well with that of Morley et al. (2017), who used the observed thermal emission of GJ 436 b to constrain its tidal heating and Q_p. With such a high Q_p, a gravitationally interacting third body in the system is not required to explain the nonzero eccentricity of GJ 436 b, as suggested by numerous authors. However, this scenario does not explain the high obliquity of the orbit reported by Bourrier et al. (2018).

We estimate an old age of $8.4^{+2.2}_{-2.0}$ Gyr for GJ 876, which hosts three outer planets in a Laplace resonance and a fourth inner planet that is not expected to interact with the resonance. This old age is surprising given that the innermost planet, GJ 876 d, orbits at only 0.02 au and has a nonzero eccentricity. We estimate a very high minimum Q_p of 5×10^5 for the $\sim 7\ M_\oplus$ planet, which suggests either that (1) GJ 876 d has a peculiar structure that is very inefficient at dissipating tidal energy; (2) GJ 876 d originally orbited farther out, where it interacted with the resonant chain and at some point fell out of resonance and migrated in; or (3) there is another unseen companion that is interacting with GJ 876 d and maintaining its nonzero eccentricity.

We thank the anonymous referee for thoughtful comments and useful suggestions.

The authors would like to thank the CARMENES consortium for making their spectra publicly available. We also thank Paul Dalba, Julie Skinner, and Todd Henry for valuable discussions during the preparation of this manuscript.

This material is based upon work supported by the National Science Foundation under grant No. 1716260. This work was partially supported by a NASA Keck PI Data Award, administered by the NASA Exoplanet Science Institute. This research made use of the NASA Exoplanet Archive, which is operated by the California Institute of Technology, under contract with the National Aeronautics and Space Administration under the Exoplanet Exploration Program.

This work made use of data from the European Space Agency (ESA) mission *Gaia* (https://www.cosmos.esa.int/gaia), processed by the *Gaia* Data Processing and Analysis Consortium (DPAC; https://www.cosmos.esa.int/web/gaia/dpac/consortium). Funding for the DPAC has been provided by national institutions, in particular the institutions participating in the *Gaia* Multilateral Agreement.

This publication made use of data products from the Two Micron All Sky Survey, which is a joint project of the University of Massachusetts and the Infrared Processing and Analysis Center/California Institute of Technology, funded by the National Aeronautics and Space Administration and the National Science Foundation.

Software: `isochrones` (Morton 2015), `emcee` (Foreman-Mackey et al. 2013), `numpy` (Oliphant 2006), `scipy` (Jones et al. 2001), `matplotlib` (Hunter 2007).

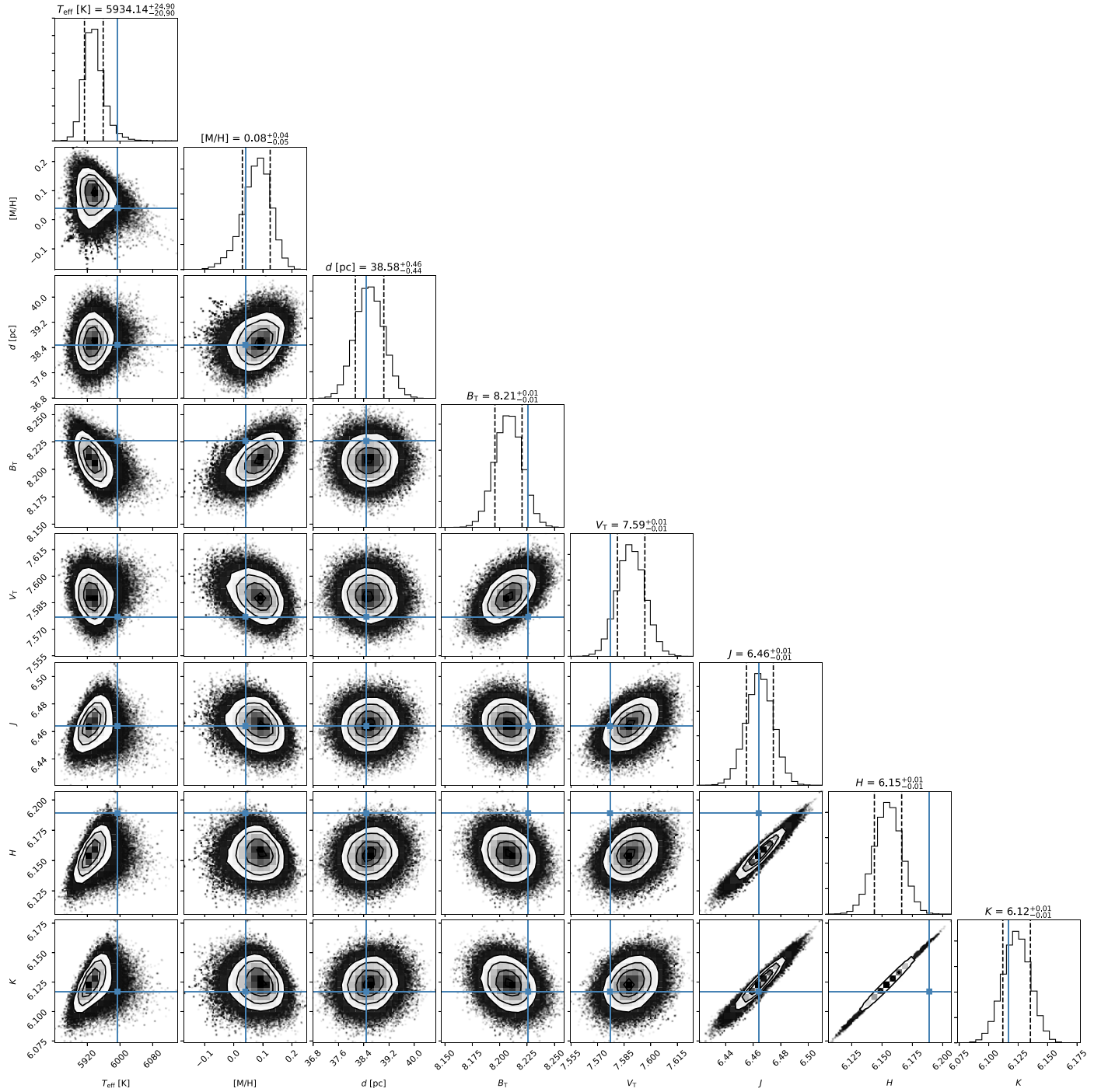

Figure 11. Corner plot showing distributions of modeled observables from sampling the posterior for HD 105. Blue crosshairs indicate measured values. The uncertainties on the observables are 80 K in $T_{\rm eff}$, 0.1 dex in [M/H], 0.015 mag in $B_{\rm T}$, 0.001 mag in $V_{\rm T}$, 0.02 mag in J, 0.023 mag in H, and 0.02 mag in $K_{\rm S}$. The observables are well reproduced by the model to within the measurement uncertainties.

Appendix
Ages of the B16 Stars

The `isochrones` package takes a number of observables along with estimates of their Gaussian uncertainties and compares them to interpolated stellar evolution models to estimate stellar parameters. In an attempt to reduce the effects of systematic differences between the stellar evolution models and spectroscopically derived parameters, we opted to include as many observables as possible with realistic absolute errors. The observables we used are $T_{\rm eff}$, [M/H], parallax, $B_{\rm T}$ magnitude, $V_{\rm T}$ magnitude, J magnitude, H magnitude, and $K_{\rm S}$ magnitude.

For $T_{\rm eff}$, we adopted the values from B16 but included a -39 K offset. The offset corresponds to the mean difference between the spectroscopic $T_{\rm eff}$ from B16 and the $T_{\rm eff}$ from optical interferometry (Boyajian et al. 2013) for stars with both measurements. Spectroscopic temperatures are not necessarily equivalent to the effective temperatures used by stellar evolution models, defined as $T_{\rm eff} = (L/4\pi R^2\sigma)^{1/4}$, where L is the luminosity and R is the radius of star. We also found that

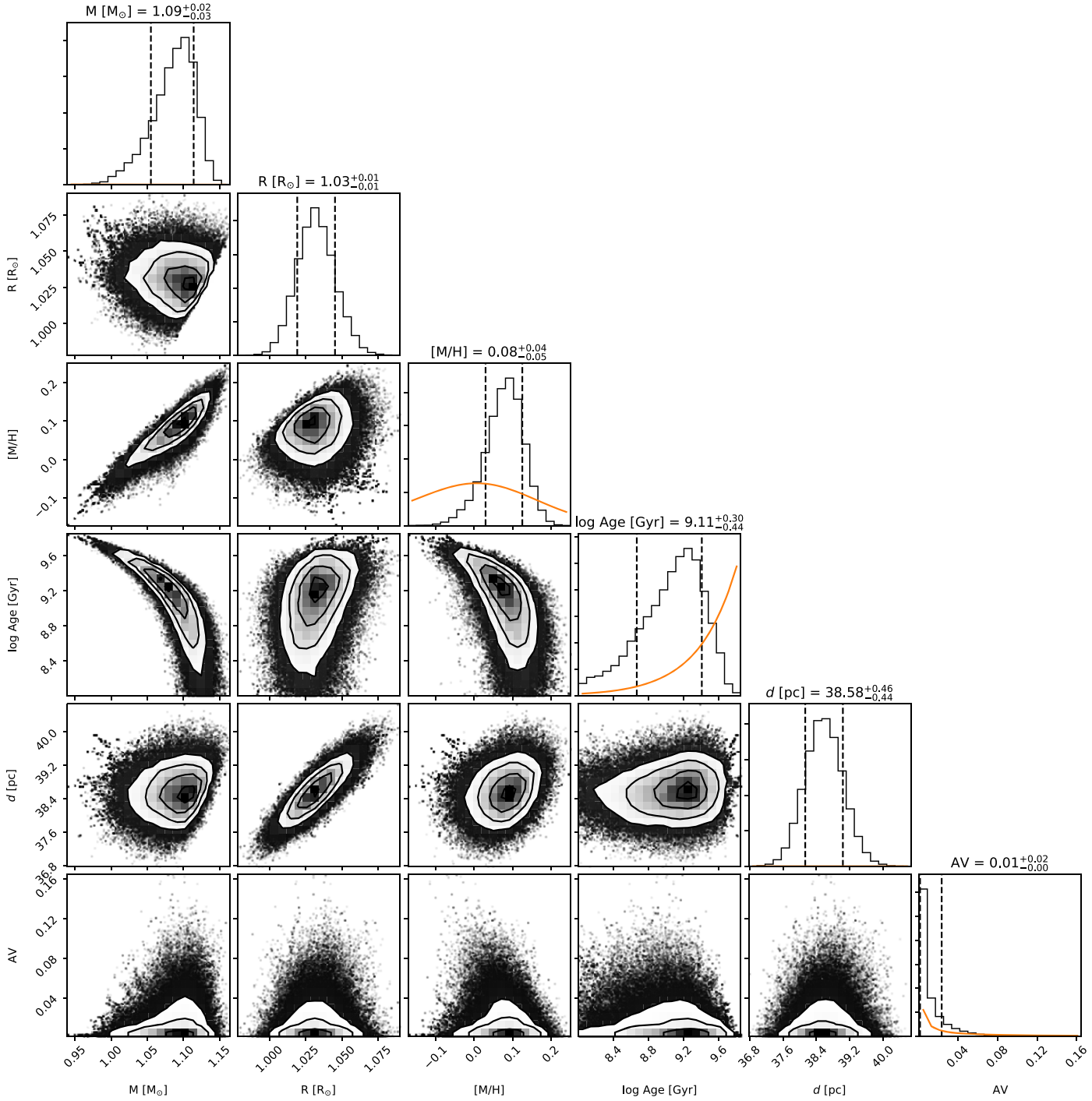

Figure 12. Corner plot showing marginalized posterior probability distributions for HD 105. Orange lines indicate the priors. Note that radius is not a model parameter.

when excluding the spectroscopic parameters and only fitting to the parallax distance and observed magnitudes, the best-fit model $T_{\rm eff}$ values were, on average, 40 K cooler than the spectroscopic temperatures. This combined with the comparison to interferometric $T_{\rm eff}$ measurements suggests that the spectroscopic $T_{\rm eff}$ values are slightly overestimated. The quoted statistical uncertainty from B16 is $\pm$25 K. We, however, used a conservative estimate of $\pm$80 K uncertainty in $T_{\rm eff}$, which corresponds to the rms scatter between spectroscopic and interferometric $T_{\rm eff}$ measurements.

For metallicity, we used the [M/H] values from B16. The MIST models assume scaled solar abundances parameterized by a single metallicity parameter. The [M/H] values of B16 represent the best-fitting solar-scaled abundances before tuning individual abundances, which is more akin to how metallicity is treated in the MIST models compared to assuming [Fe/H] as the metallicity. The B16 quoted statistical uncertainty on [M/H] is 0.01 dex. We adopt an uncertainty of 0.1 dex in order to account for various systematic errors, such as differences in the assumed solar abundances of B16 (Grevesse et al. 2007)

and the MIST models (Asplund et al. 2009) and systematic error from the simple assumption of scaled solar abundances.

We cross-matched the B16 sample with the HIPPARCOS (ESA 1997) and *Gaia* DR1 TGAS (Gaia Collaboration et al. 2016b, 2016a; Lindegren et al. 2016) catalogs. When available, we used *Gaia* parallaxes and quoted uncertainties. If *Gaia* data were not available, we used HIPPARCOS parallaxes with quoted uncertainties.

We included five magnitudes with their quoted uncertainties. We included B_T and V_T magnitudes from the Tycho-2 catalog (Høg et al. 2000) and J, H, and K_S magnitudes from 2MASS (Skrutskie et al. 2006).

We made two changes to the `isochrones` package. First, we implemented a Jefferys prior for A_V within the bounds $0.001 < A_V < 1$. Second, we implemented an `Isochrone` class for the MIST models, as opposed to the default `FastIsochrone` class. We found that the interpolation scheme used in the `FastIsochrone` class produced strange artifacts, such as striations in 2D marginalized posteriors. The `Isochrone` class uses the `scipy.interpolate.LinearNDInterpolator` function to interpolate the models. To speed up computing, we calculate the Delaunay triangulation only for age >0.1 Gyr, [M/H] > -1, and $0.5 < M/M_\odot < 1.5$, which encompasses our entire FGK sample after making the cuts described in Section 3.2.3.

For each star, we used the `emcee` python module (Foreman-Mackey et al. 2013) to sample the posterior with an affine-invariant ensemble sampler (Goodman & Weare 2010). We used 100 walkers with 2000 burn-in steps and 5000 sampling steps. We initialized the walkers based on parameter estimates that maximized the posterior. We removed chains with an acceptance fraction <0.1 and excluded from further analysis any star whose maximum integrated autocorrelation time is greater than $1/3$ of the number of sampling steps. Figures 11 and 12 show corner plots for the modeled observables and model parameters, respectively, for one representative star, HD 105. The input observables are well reproduced by the models to within the measurement uncertainties. We take the median of the marginalized age posterior as the best-fit age.

ORCID iDs

Mark J. Veyette https://orcid.org/0000-0002-0385-2183
Philip S. Muirhead https://orcid.org/0000-0002-0638-8822

References

Agüeros, M., Bowsher, E., Bochanski, J., et al. 2018, ApJ, 862, 33
Allard, F. 2016, in Proc. Annual meeting of the French Society of Astronomy and Astrophysics, SF2A-2016, ed. C. Reylé et al. (Lyon: Société Francaise d'Astronomie et d'Astrophysique), 223
Allard, F., Homeier, D., & Freytag, B. 2012, RSPTA, 370, 2765
Almeida-Fernandes, F., & Rocha-Pinto, H. J. 2018, MNRAS, 476, 184
Asplund, M., Grevesse, N., Sauval, A. J., & Scott, P. 2009, ARA&A, 47, 481
Astudillo-Defru, N., Forveille, T., Bonfils, X., et al. 2017, A&A, 602, A88
Attridge, J. M., & Herbst, W. 1992, ApJL, 398, L61
Baraffe, I., Homeier, D., Allard, F., & Chabrier, G. 2015, A&A, 577, A42
Barnes, R. 2015, IJAsB, 14, 321
Barnes, S. A. 2003, ApJ, 586, 464
Barnes, S. A., Weingrill, J., Fritzewski, D., Strassmeier, K. G., & Platais, I. 2016, ApJ, 823, 16
Batygin, K., Deck, K. M., & Holman, M. J. 2015, AJ, 149, 167
Batygin, K., Laughlin, G., Meschiari, S., et al. 2009, ApJ, 699, 23
Bedell, M., Bean, J. L., Melendez, J., et al. 2018, arXiv:1802.02576
Benedict, G. F., Henry, T. J., Franz, O. G., et al. 2016, AJ, 152, 141
Bensby, T., Feltzing, S., & Oey, M. S. 2014, A&A, 562, A71
Beust, H., Bonfils, X., Montagnier, G., Delfosse, X., & Forveille, T. 2012, A&A, 545, A88
Bonfils, X., Delfosse, X., Udry, S., et al. 2005a, A&A, 442, 635
Bonfils, X., Delfosse, X., Udry, S., et al. 2013, A&A, 549, A109
Bonfils, X., Forveille, T., Delfosse, X., et al. 2005b, A&A, 443, L15
Bourrier, V., Lovis, C., Beust, H., et al. 2018, Natur, 553, 477
Boyajian, T. S., von Braun, K., van Belle, G., et al. 2013, ApJ, 771, 40
Brewer, J. M., Fischer, D. A., Valenti, J. A., & Piskunov, N. 2016, ApJS, 225, 32
Buder, S., Lind, K., Ness, M. K., et al. 2018, arXiv:1804.05869
Butler, R. P., Johnson, J. A., Marcy, G. W., et al. 2006, PASP, 118, 1685
Butler, R. P., Vogt, S. S., Marcy, G. W., et al. 2004, ApJ, 617, 580
Caballero, J. A., Guàrdia, J., López del Fresno, M., et al. 2016, Proc. SPIE, 9910, 99100E
Casagrande, L., Schönrich, R., Asplund, M., et al. 2011, A&A, 530, A138
Choi, J., Dotter, A., Conroy, C., et al. 2016, ApJ, 823, 102
De Silva, G. M., Freeman, K. C., Bland-Hawthorn, J., Asplund, M., & Bessell, M. S. 2007, AJ, 133, 694
Demory, B.-O., Gillon, M., Barman, T., et al. 2007, A&A, 475, 1125
Dotter, A. 2016, ApJS, 222, 8
Douglas, S. T., Agüeros, M. A., Covey, K. R., & Kraus, A. 2017, ApJ, 842, 83
Dressing, C. D., & Charbonneau, D. 2013, ApJ, 767, 95
Dressing, C. D., & Charbonneau, D. 2015, ApJ, 807, 45
Eggen, O. J. 1998, AJ, 115, 2453
ESA 1997, in ESA Special Publication, Vol. 1200, The HIPPARCOS and TYCHO Catalogues. Astrometric and Photometric Star Catalogues Derived from the ESA HIPPARCOS Space Astrometry Mission (Noordwijk: ESA), 1200
Feltzing, S., & Holmberg, J. 2000, A&A, 357, 153
Feng, Y. K., Wright, J. T., Nelson, B., et al. 2015, ApJ, 800, 22
Feuillet, D. K., Bovy, J., Holtzman, J., et al. 2016, ApJ, 817, 40
Feuillet, D. K., Bovy, J., Holtzman, J., et al. 2018, MNRAS, 477, 2326
Foreman-Mackey, D., Hogg, D. W., Lang, D., & Goodman, J. 2013, PASP, 125, 306
Forveille, T., Bonfils, X., Delfosse, X., et al. 2009, A&A, 493, 645
Fuhrmann, K. 1998, A&A, 338, 161
Gagné, J., Mamajek, E. E., Malo, L., et al. 2018, ApJ, 856, 23
Gaia Collaboration, Brown, A. G. A., Vallenari, A., et al. 2016a, A&A, 595, A2
Gaia Collaboration, Brown, A. G. A., Vallenari, A., et al. 2018, arXiv:1804.09365
Gaia Collaboration, Prusti, T., de Bruijne, J. H. J., et al. 2016b, A&A, 595, A1
Gaidos, E., Mann, A. W., Kraus, A. L., & Ireland, M. 2016, MNRAS, 457, 2877
Gaidos, E., Mann, A. W., Lépine, S., et al. 2014, MNRAS, 443, 2561
Garraffo, C., Drake, J. J., & Cohen, O. 2015, ApJ, 813, 40
Garraffo, C., Drake, J. J., Dotter, A., et al. 2018, ApJ, 862, 90
Goldreich, P., & Soter, S. 1966, Icar, 5, 375
Goodman, J., & Weare, J. 2010, CAMCS, 5, 65
Grevesse, N., Asplund, M., & Sauval, A. J. 2007, SSRv, 130, 105
Hawkins, K., Masseron, T., Jofré, P., et al. 2016, A&A, 594, A43
Haywood, M., Di Matteo, P., Lehnert, M. D., Katz, D., & Gómez, A. 2013, A&A, 560, A109
Henning, W. G., O'Connell, R. J., & Sasselov, D. D. 2009, ApJ, 707, 1000
Høg, E., Fabricius, C., Makarov, V. V., et al. 2000, A&A, 355, L27
Howard, A. W., Johnson, J. A., Marcy, G. W., et al. 2010, ApJ, 721, 1467
Hunter, J. D. 2007, CSE, 9, 90
Ioannou, P. J., & Lindzen, R. S. 1993, ApJ, 406, 252
Irwin, J., Berta, Z. K., Burke, C. J., et al. 2011, ApJ, 727, 56
Irwin, J., Hodgkin, S., Aigrain, S., et al. 2007, MNRAS, 377, 741
Jackson, B., Barnes, R., & Greenberg, R. 2009, ApJ, 698, 1357
Jackson, B., Greenberg, R., & Barnes, R. 2008, ApJ, 678, 1396
Johnson, J. A., Aller, K. M., Howard, A. W., & Crepp, J. R. 2010a, PASP, 122, 905
Johnson, J. A., & Apps, K. 2009, ApJ, 699, 933
Johnson, J. A., Howard, A. W., Marcy, G. W., et al. 2010b, PASP, 122, 149
Jones, E., Oliphant, T., Peterson, P., et al. 2001, SciPy: Open Source Scientific Tools for Python
Kane, S. R., Ciardi, D. R., Gelino, D. M., & von Braun, K. 2012, MNRAS, 425, 757
Kane, S. R., von Braun, K., Henry, G. W., et al. 2017, ApJ, 835, 200
Kipping, D. M. 2013, MNRAS, 434, L51
Lainey, V., Arlot, J.-E., Karatekin, Ö, & van Hoolst, T. 2009, Natur, 459, 957
Lainey, V., Dehant, V., & Pätzold, M. 2007, A&A, 465, 1075
Lainey, V., Karatekin, Ö., Desmars, J., et al. 2012, ApJ, 752, 14
Lainey, V., Jacobson, R. A., Tajeddine, R., et al. 2017, Icar, 281, 286

Laughlin, G., Bodenheimer, P., & Adams, F. C. 1997, ApJ, 482, 420
Laughlin, G., Bodenheimer, P., & Adams, F. C. 2004, ApJL, 612, L73
Lindegren, L., Hernandez, J., Bombrun, A., et al. 2018, A&A, 616, A2
Lindegren, L., Lammers, U., Bastian, U., et al. 2016, A&A, 595, A4
Maciejewski, G., Niedzielski, A., Nowak, G., et al. 2014, AcA, 64, 323
Mamajek, E. E., & Hillenbrand, L. A. 2008, ApJ, 687, 1264
Maness, H. L., Marcy, G. W., Ford, E. B., et al. 2007, PASP, 119, 90
Mann, A. W., Brewer, J. M., Gaidos, E., Lépine, S., & Hilton, E. J. 2013, AJ, 145, 52
Mann, A. W., Feiden, G. A., Gaidos, E., Boyajian, T., & von Braun, K. 2015, ApJ, 804, 64
Mann, A. W., Feiden, G. A., Gaidos, E., Boyajian, T., & von Braun, K. 2016, ApJ, 819, 87
Marcy, G. W., Butler, R. P., Fischer, D., et al. 2001, ApJ, 556, 296
Marcy, G. W., Butler, R. P., Vogt, S. S., Fischer, D., & Lissauer, J. J. 1998, ApJL, 505, L147
Mardling, R. A. 2008, arXiv:0805.1928
Martí, J. G., Giuppone, C. A., & Beaugé, C. 2013, MNRAS, 433, 928
Martig, M., Rix, H.-W., Aguirre, V. S., et al. 2015, MNRAS, 451, 2230
Mayor, M., Bonfils, X., Forveille, T., et al. 2009, A&A, 507, 487
McQuillan, A., Aigrain, S., & Mazeh, T. 2013, MNRAS, 432, 1203
Meibom, S., Barnes, S. A., Platais, I., et al. 2015, Natur, 517, 589
Millholland, S., Laughlin, G., Teske, J., et al. 2018, AJ, 155, 106
Montes, D., López-Santiago, J., Gálvez, M. C., et al. 2001, MNRAS, 328, 45
Morley, C. V., Knutson, H., Line, M., et al. 2017, AJ, 153, 86
Morton, T. D. 2015, Isochrones: Stellar Model Grid Package, Astrophysics Source Code Library, ascl:1503.010
Morton, T. D., & Swift, J. 2014, ApJ, 791, 10
Muirhead, P. S., Mann, A. W., Vanderburg, A., et al. 2015, ApJ, 801, 18
Murray, C. D., & Dermott, S. F. 2000, Solar System Dynamics (Cambridge: Cambridge Univ. Press)
Newton, E. R., Irwin, J., Charbonneau, D., et al. 2016, ApJ, 821, 93
Newton, E. R., Irwin, J., Charbonneau, D., et al. 2017, ApJ, 834, 85
Nissen, P. E. 2015, A&A, 579, A52
Nordström, B., Mayor, M., Andersen, J., et al. 2004, A&A, 418, 989
Ogilvie, G. I., & Lin, D. N. C. 2004, ApJ, 610, 477
Oliphant, T. 2006, A Guide to NumPy, https://www.scipy.org/citing.html
Pedregosa, F., Varoquaux, G., Gramfort, A., et al. 2011, Journal of Machine Learning Research, 12, 2825
Pepper, J. 2018, RNAAS, 2, 14
Pepper, J., Pogge, R. W., DePoy, D. L., et al. 2007, PASP, 119, 923
Quirrenbach, A., Amado, P. J., Caballero, J. A., et al. 2014, Proc. SPIE, 9147, 91471F
Rasio, F. A., & Ford, E. B. 1996, Sci, 274, 954
Rebull, L. M., Stauffer, J. R., Hillenbrand, L. A., et al. 2017, ApJ, 839, 92
Reiners, A., Ribas, I., Zechmeister, M., et al. 2018a, A&A, 609, L5
Reiners, A., Zechmeister, M., Caballero, J. A., et al. 2018b, A&A, 612, A49
Ribas, I., Font-Ribera, A., & Beaulieu, J.-P. 2008, ApJL, 677, L59
Rivera, E. J., Laughlin, G., Butler, R. P., et al. 2010, ApJ, 719, 890
Rivera, E. J., Lissauer, J. J., Butler, R. P., et al. 2005, ApJ, 634, 625
Rodriguez, D. 2016, dr-rodriguez/Kinematics-App: Stellar Kinematics, v1.0, Zenodo, doi:10.5281/zenodo.192159
Rojas-Ayala, B., Covey, K. R., Muirhead, P. S., & Lloyd, J. P. 2010, ApJL, 720, L113
Skrutskie, M. F., Cutri, R. M., Stiening, R., et al. 2006, AJ, 131, 1163
Spina, L., Meléndez, J., Karakas, A. I., et al. 2016, A&A, 593, A125
Stauffer, J. R., Schultz, G., & Kirkpatrick, J. D. 1998, ApJL, 499, L199
Suárez Mascareño, A., González Hernández, J. I., Rebolo, R., et al. 2017a, A&A, 597, A108
Suárez Mascareño, A., González Hernández, J. I., Rebolo, R., et al. 2017b, A&A, 605, A92
Swift, J. J., Johnson, J. A., Morton, T. D., et al. 2013, ApJ, 764, 105
Tabernero, H. M., Montes, D., González Hernández, J. I., & Ammler-von Eiff, M. 2017, A&A, 597, A33
Tong, X., & Zhou, J. 2009, ScChG, 52, 640
Trifonov, T., Kürster, M., Zechmeister, M., et al. 2018, A&A, 609, A117
Udry, S., Bonfils, X., Delfosse, X., et al. 2007, A&A, 469, L43
Veyette, M. J., Muirhead, P. S., Mann, A. W., et al. 2017, ApJ, 851, 26
Veyette, M. J., Muirhead, P. S., Mann, A. W., & Allard, F. 2016, ApJ, 828, 95
Vican, L. 2012, AJ, 143, 135
Weiss, L. M., Marcy, G. W., Rowe, J. F., et al. 2013, ApJ, 768, 14
Wolfgang, A., & Lopez, E. 2015, ApJ, 806, 183
Wolfgang, A., Rogers, L. A., & Ford, E. B. 2016, ApJ, 825, 19
Wright, D. J., Wittenmyer, R. A., Tinney, C. G., Bentley, J. S., & Zhao, J. 2016, ApJL, 817, L20
Zechmeister, M., Anglada-Escudé, G., & Reiners, A. 2014, A&A, 561, A59
Zhang, K., & Hamilton, D. P. 2008, Icar, 193, 267